COLOUR SENSITIVE LENS-LESS IMAGING

USING RESONATING NANOPHOTONIC DIFFRACTION GRATINGS

COLOUR SENSITIVE LENS-LESS IMAGING

USING RESONATING NANOPHOTONIC DIFFRACTION GRATINGS

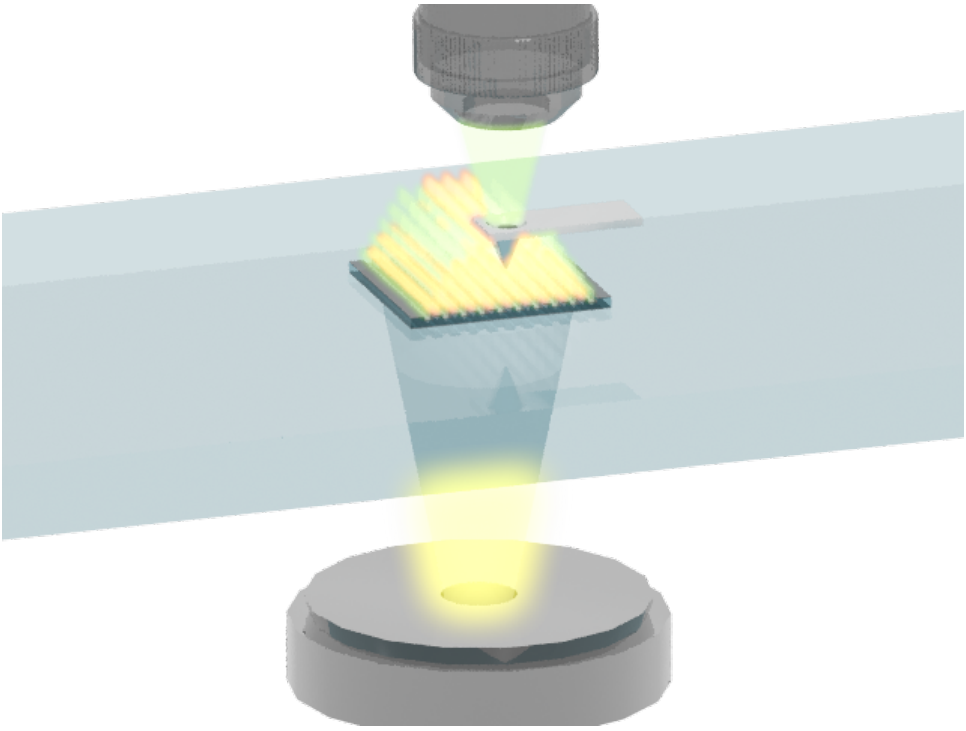

Master's Thesis

for acquiring the degree of Master of Science
in Electrical Engineering at Delft University of Technology,

by

Adriaan Johannes TAAL

Student Signals and Systems,
Delft University of Technology, The Netherlands

This master's thesis will be defended on May 22nd for the following Jury:

Prof. dr. E. Charbon,	Delft University of Technology
dr. C. Lee,	Columbia University
Independent members:	
Prof. dr. A. Theuwissen	Delft University of Technology
Prof. dr. S. Stallinga	Delft University of Technology

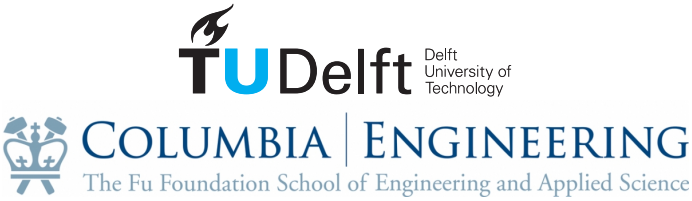

Keywords: Lens-less imaging, nanophotonics, nanofabrication, sparse reconstruction, fourier domain capture, camera miniaturization

Front: NSOM measurement 3D visualization. Credits to Changhyuk Lee

ABSTRACT

This thesis presents a novel nanophotonic Metal-Insulator-Metal (MIM) grating structure that diffracts incident light by filtering colour based on interference. The grating creates two independent self-images (Talbot patterns) for two almost arbitrarily tuneable wavelengths in the visible spectrum.

Lens-less imaging is promising for its ability to be implemented in extremely small image sensors. Physical dimensions of lenses are prohibiting image sensors to scale with CMOS scaling trends. The grating substitutes a physical part of the angle sensitive pixel (ASP), a method for lens-less imaging.

It is explored that by postprocessing this structure on top of a digital pixel array, colour sensitivity is added to the previously monochromatic angle sensitive pixel lens-less imaging method. Where multichromatic scenes would previously deteriorate ASP array reconstruction quality, the proposed MIM ASP uses the wavelength dimension to its advantage.

The thesis states that using a patterned nanophotonic Metal-Insulator-Metal structure that filters colour based on interference on top of a pixel array, lensless imaging in near-field scenario's takes a step forward by adding high Q-factor wavelength separation, opening a new dimension of distinguishability without compromising SNR.

CONTENTS

1

BACKGROUND

This chapter introduces the reader into the relevance of lensless imaging. Two very distinct methods for creating small form factor spatial discrimination are presented. It motivates further investigation into angle sensitive pixels, a certain implementation of lensless imaging.

1.1. LENS-BASED IMAGING

For most people I talk to about my research, lens-less imaging sounds unprobable. How can an image be created without a lens, and what is the motivation for doing so? Actually, the world's first camera's did not have something as sophisticated as a lens. Pinhole camera's, as they were known by, operated by having a small aperture placing each point from the object plane on a unique point on the sensitive area inside the camera. The sharpness of the image is inversely proportional to the aperture radius. However, signal intensity is quadratically inversely proportional to the aperture radius, thus sharp imaging would end up with low contrast (SNR) or take infeasibly long to create.

Lenses were devised to anhilliate this problem. As seen in figure 1.1, light reaching the area of the entire photosensitive area is gathered while still being uniquely mapped to the photosensitive area, given that the photosensitive area is on the focal distance of the lens. Even though chemical (a.k.a. analog) camera's are replaced for digital camera's in virtually every commercial application, the lens has survived, for very good reasons which will be touched upon. As such, we grow up equating an image sensor with a lens-based implementation.

Since the release of the first CPU, the Intel 4004 in 1971, Moore's law has pushed semiconductor companies to scale down minimum feature sizes in order to stay ahead of the competition. Although physical limits are bound to be hit in the near future, the number of transistors per unit area has doubled every two years. Nowadays most digital camera's are implemented in CCD or APS architectures [2], and as such, we see digital pixel density scaling almost solely driven by transistor size scaling. Other drivers such as

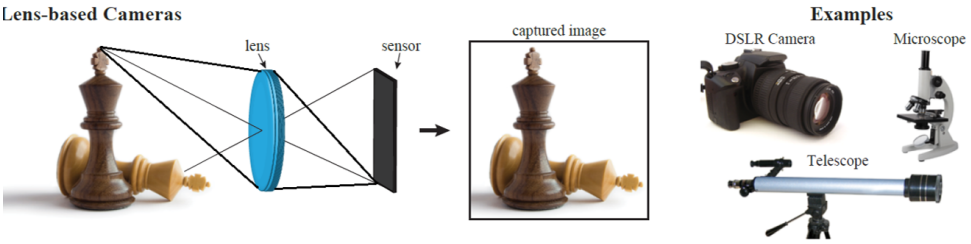

Figure 1.1: Lens-based imaging system [1]. The sensor directly captures the scene due to the unique mapping function of the lens.

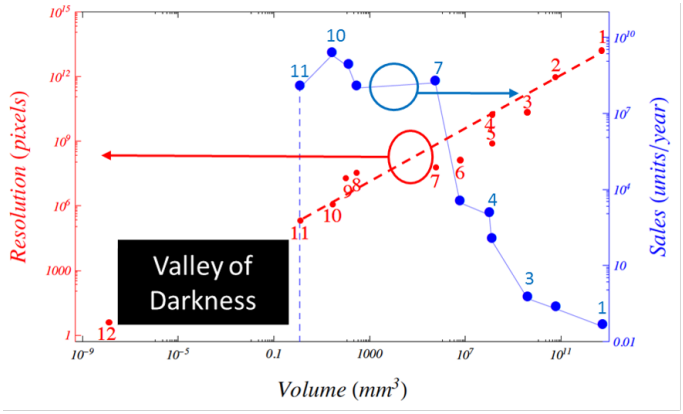

Figure 1.2: Prediction of market potential of extremely small image sensors [3]. Possible markets for small volume image sensors could be authentication by facial recognition, biomedical, or distributed sensing.

increasing manufacturing capabilities has led to innovations such as microlenses which increase the gathered signal strength even further. Eventually this pixel size will be limited not only by the diffraction limit, but also by noise, and the penetration depth of photons in the semiconductor. Manufacturing limits the aspect ratio thus the depth of the active area.

There is a caveat to these beautiful trends. While the pixel size decreases, the image sensor size hasn't decreased as strongly. The total image sensor volume is restricted by the size of the lens which is restricted by manufacturing. Figure 1.2 shows a large potential for sales volume when the image sensor volume size enters the empty area coined as the valley of darkness.

1.2. MOTIVATION FOR LENSLESS IMAGING

Instead of waiting for lens manufacturing to drive scaling, lensless imaging is a promising alternative for certain application. This paragraph will elaborate why lensless imaging is almost exclusively driven by the much more rapid scaling of transistor feature size.

Figure 1.3 shows the required parts of lensless imaging. At first, a structure needs to

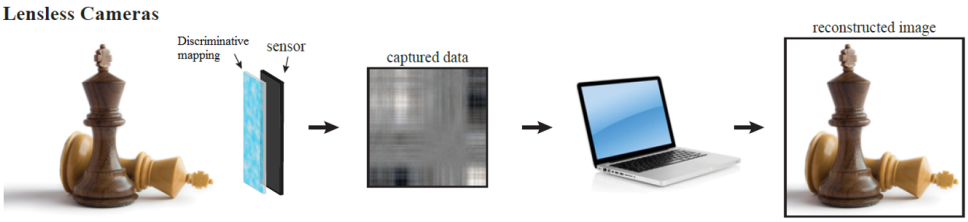

Figure 1.3: Lens-less imaging system [1]. Advances in computational speed can substitute parts of the image sensor that have previously required a physical structure. By implementing a discriminative mapping on the sensor, the image sensor captures data which by undoing the mapping in software or directly on chip.

be designed that can discrimininatively map parts of the scene to different parts of the sensor. This mapping does not need to be unique, as fundamental signal processing theory states that a many-to-many mapping can reconstruct perfectly, given there are more detectors than sources. Even though for natural scenes this constraint is never met, an application later in this thesis will make use of such a scenario. The mapping does not need to be in the spatial domain either. It will be shown that directly capturing fourier coefficients from the scene also leads to ability to reconstruct. The only requirement to this mapping is to implement a different mapping for each set of pixels to gather as much as information from the scene as possible.

Advancements in computational speed and ease of programming of the last decade have made large scale frame-to-frame reconstruction algorithms possible. Although all reconstruction demonstrations in this thesis are done on PC in Matlab, methods exist to port mathematical programming to fully layouted digital logic.

Therefore, by continuously shifting a larger parts of the image creation from the optoelectronic domain into the computational domain, designers can choose to trade pixels for computation. Remember that pixels will be larger than the diffraction limit, which is 175nm in SiO2 for green light (525nm), which can be traded for many transistors in the current state of the art, Samsung's 10nm node. The only limitation will be in the area consumption of the transistor implementation of the most efficient reconstruction algorithm.

1.3. IMPLEMENTING LENSLESS IMAGING

Figure 1.4 shows three published methods of achieving a discriminative mapping required to substitute a lens. Lensless imaging using coded aperture [4] was required for large scale X-ray and Gamma ray imaging figure 1.4a, at whose frequencies materials with the correct refractive index properties are expensive or otherwise infeasible. Each source casts a specific pattern over multiple, defined by the coded mask. The total from which the source locations can be calculated, and thus an image reconstructed. This concept also goes by the name of compressive sensing [5]. Building upon a similar idea, Rice University built FlatCam, figure 1.4b. This consist of multiple pinholes in a mask laid over a photodiode array [6]. The mask is designed in such a way to tradeoff information extraction per pixel and reconstructive computational simplicity. The drawback

1

with the coded aperture method however, is the required separation between mask and detector. This separation is needed to cast the pattern on multiple pixels. The thickness does scale with the sensor width and length, but will always keep a cube sized volume. In other words, for the proposed 500um separation, a new constraint is introduced on the order of the smallest lens-based sensors (figure 1.2), meaning little net gain.

As will be the topic of next section, the Cornell Molnar group devised angle sensitive pixels (ASP's) based on diffraction gratings to discriminate incident light in the spatial domain (figure 1.4c). Such an ASP is implemented in CMOS without postprocessing [7], promising thicknesses that scale with semiconductor company manufacturing techniques. Therefore this thesis takes the path into lensless imaging using angle sensitive pixels.

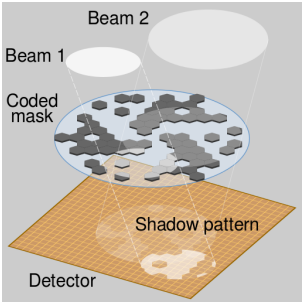

(a) NASA coded aperture shadow imaging for X-ray imaging [4].

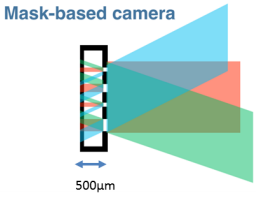

(b) Rice University FlatCam [6]

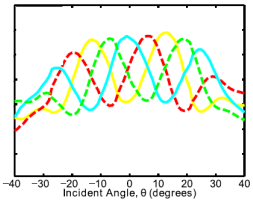

(c) Cornell Molnar group diffraction based angle sensitive pixel [7]

Figure 1.4: Lensless imaging methods. Method (a) is a coded aperture shadow masking created by NASA for X-ray imaging. Method (b) is similar to (a), with feature size adapted to the visible spectrum. Method (c) uses diffraction gratings to modulate the angle of incident light to recorded intensity on the photodiode.

2

ANGLE SENSITIVE PIXEL

This chapter introduces the reader into physics fundamental to angle sensitive pixels. For engineers, tuneability is crucial and therefore explored using simulation. Using the same simulation, it is shown that current state of the art in angle sensitive pixel design fails for colour imaging, which in turn completes the motivation for this thesis research.

2.1. PHYSICS OF DIFFRACTION BASED ASP

Figure 2.1 shows how the angle sensitive pixel is implemented in CMOS. A monochromatic plane wave source is launched onto the structure. The amplitude grating creates a talbot self-image [8-9], with maximum intensities predicted by equation 2.1 [10], known as the half integer talbot depths. This distance is a function of grating pitch (**p**), wavelength (λ), and refractive index (**n**) of the intermediate insulator.

$$Z_{T,k} = k\left[\frac{nd^2}{\lambda} - \frac{\lambda}{4n}\right] \tag{2.1}$$

The secondary grating, or analyzer grating, selectively transmits or blocks the Talbot pattern. This analyzer grating is placed at a grating separation (**d**), optimally at an integer talbot order $d = Z_{T,k}$. By changing the angle of the incident light, the talbot pattern shifts laterally. This creates a cosine shaped modulation effect as depicted in figure 2.2.

2.2. CHARACTERIZATION OF WIRE GRATING ASP

The cosine shaped modulation is parameterized by three variables in equation 2.2. As stated in chapter 1, each pixel should have a different response in order to extract different information from the scene. In the ideal, noiseless, errorless case, no redundancy is needed, and each pixel could have a different parameterization. Therefore the range of tuning is investigated, and table 2.1 shows how to achieve tuning.

$$I(\theta) = I(\theta = 0)\left[1 + m\cos\left(\beta\theta + \alpha\right)\right] \tag{2.2}$$

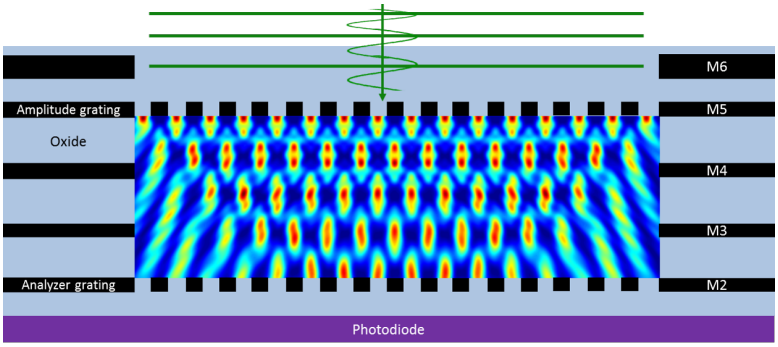

Figure 2.1: Angle sensitive pixel design using diffraction gratings. The amplitude grating creates a talbot self-image with maximum intensities predicted by equation 2.1. The secondary grating, or analyzer grating, selectively transmits or blocks the Talbot pattern. By changing the angle of the incident light, the talbot pattern shifts laterally.

Even though the modulation index cannot be tuned directly, it is extremely important as it directly relates to detector SNR. In the ideal case, m equals 1, meaning perfect transmission of peak angles of design, and perfect rejection of angles at the cosine mimima. With this perfect rejection, the largest spatial discrimination is achieved for each detector and thus the most information retrieved from the scene. When m is smaller than unity, an unmodulated response (DC voltage) appears in its angular response function. This DC is then uniform over incident angle which adds zero information. The signal energy $I(0)[1-m]$ is essentially discarded. Equation 2.3 shows how SNR is implemented during image reconstruction in chapter 6.

$$SNR = \frac{\sigma_s^2}{\sigma_n^2} = \frac{I(0)m}{\sigma_n^2} \tag{2.3}$$

In order to verify claims and lay the foundation for correct future simulation, tuning βas a function of the pitch (**p**) was simulated in Lumerical FDTD solutions and plotted in figure 2.3. This commercially available software package is a numerical Finite Difference Time Domain solver for maxwell equations. The result shows coherence with the model prediction, indicating correct simulation setup. See appendix for details.

DISCUSSION ON ASP TUNING

There are a few remarks on the tuning space.

- In a technology node, the grating separation (**d**) is fixed to the height separation of any combination of available metal layers. This implies that certain combinations of wavelength (λ) and pitch (**p**) are not useful as they place the analyzer grating at a transition between talbot orders. This results in low modulation index.
- As modeled in [7], a pixel with width **w** should contain at least 12 grating periods in order to have high modulation index. Figure 2.1 shows how each talbot order increase does reduce the amount of correctly formed locations of maximum intensity by 2.
- Intensity of incident angles higher than approximately 45 degrees are not modulated perfectly anymore, and instead roll off (see figure 2.2). This maximum angle of correct modulation is referred to as the deadangle and is caused by the aspect ratio of the metal stack above the amplitude grating. This could be modeled by for example a raised cosine window multiplied with the modulated angular response.

ASP GRATING DESIGN FLOW

The following flow summarized parameterized grating design for an ASP array.

1. Determine application specific required layout of β per pixel for best scene reconstruction [11]
2. Determine source wavelength λ
3. Determine what β can be achieved with optimal modulation index by available grating separation distances
4. Vary pitch and grating separation to implement required β
5. Apply offset α freely where required

But if the source wavelength is the fundamental, unchangeable constant in design, how is the response affected by a spectrally varying source?

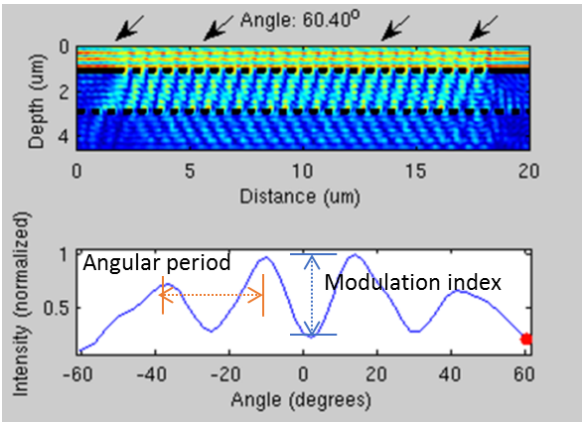

Figure 2.2: Modulation of incoming light. The ASP is characterized by its angular frequency, the angular offset of the peak from zero incidence and its modulation index.

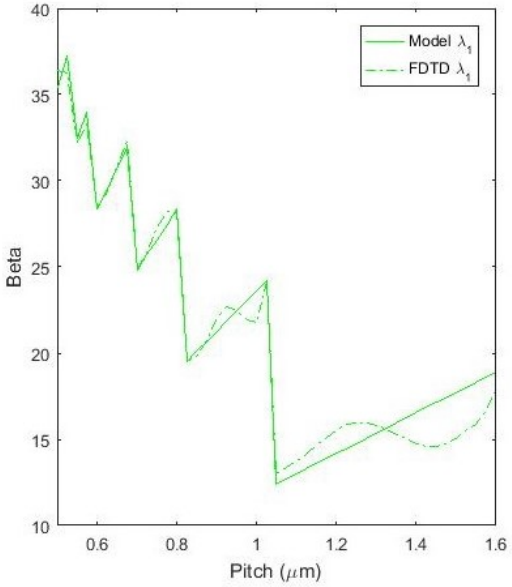

Figure 2.3: FDTD simulation reproduction of tuning in the ASP [7]. The simulation is done for a wavelength of 532nm, with grating separtion at the fourth talbot order. The grating material is a Perfect Electrical Conductor, to idealize reflection. The separation material is SiO2.

Table 2.1: Tuning of the angle sensitive pixel. The wider the reliable range of tuning, the larger the diversity of pixel information extraction. Because the gratings are implemented in a certain technology node, the design rule checking (DRC) constraints play a role. These are omitted however. Note that **w** is used for photodetector width. Also note that throughout the entire thesis, the duty cycle is kept at 50% for ease of analysis.

Tuned Parameter	**By adjusting**	**Modeled**	**Lower bound**	**Upper bound**
Angular frequency β	pitch (**p**), see figure 2.3, and talbot order (**k**)	$\beta = \frac{2\pi}{np} \cdot m \left[\frac{nd^2}{\lambda} - \frac{\lambda}{4n} \right]$	$p \geq \frac{\lambda}{2n}$	$p \leq \frac{w}{12}$ [7]
Offset α	lateral grating offset (**l**)	$\alpha = 2\pi \frac{l}{p}$	0	2π
Modulation index m	select grating separation at talbot order (**d**)	$m = \frac{\max I(\theta) - \min I(\theta)}{\max I(\theta)}$	0	0.8 [7]

2.3. LIMITATION OF ASP

To illustrate the distortion in ASP function, a talbot carpet is simulated in FDTD for two wavelengths using the same talbot grating. A wavelength increase of 10% places the talbot distance 10% closer. The simulation in figure 2.4 illustrates the distortive effect of such spectral variation.

This analysis is expanded in figure 2.5. It can be concluded that current ASP strongly suffers from its wavelength dependency. Variations in $\beta$are detrimental to reconstruction quality, as will be demonstrated in chapter 6.

A naive solution would be to bandpass filter incident light in a small bandwidth of 75nm around the optimum wavelength. Even with a nanostructured filter transmission of 50% [12], the ideal ASP doesn't harvest more than % 12.5 [7] of incident light. By trying to solve one problem, another problem is introduced. Furthermore, to implement a full visible spectrum sensor using RGGB (Bayer Tiling, [12]), four subpixels are required. This is area inefficient. This illustrates a clear need to redesign the ASP structure for colour imaging, and concludes the motivation for the research in this thesis.

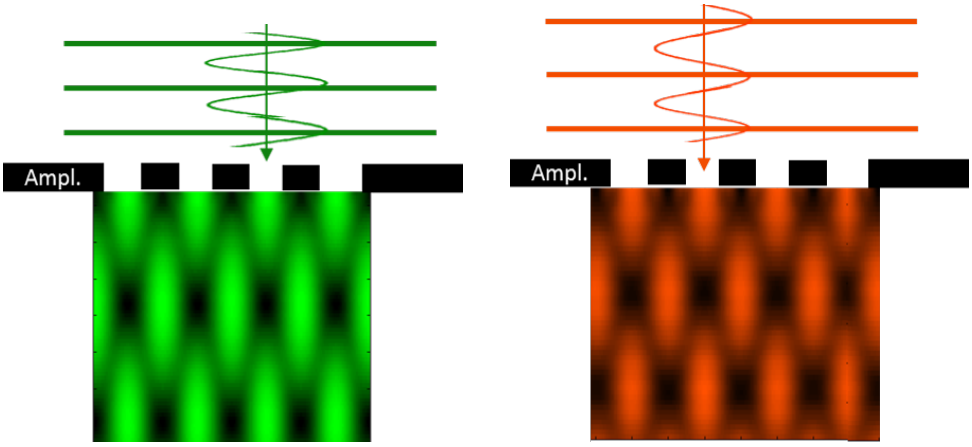

(a) λ= 532nm, optimal placement (b) λ= 600nm, non-optimal placement

Figure 2.4: FDTD simulation of the talbot carpet formed by two different incident wavelengths. The grating pitch is 1µm, the simulated cross-section area is 4µm x 4µm. While the green image shows intensity maximum, the orange talbot image transitions to a next order at the bottom of the simulation. Placing an analyzer grating at that distance creates distorted modulation in the orange case.

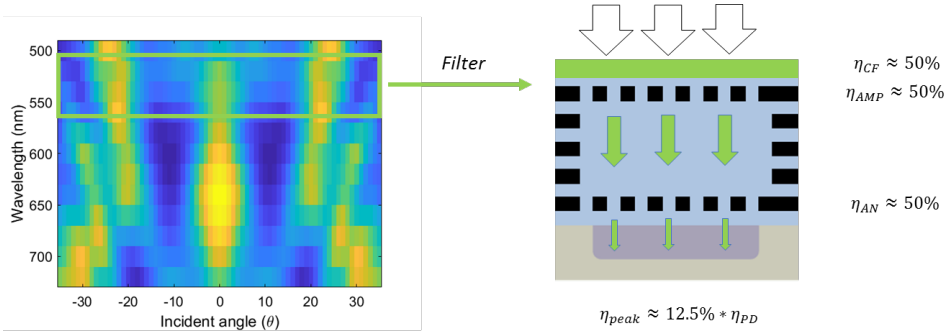

Figure 2.5: FDTD simulation of the angular response versus incident wavelength for an ASP optimized at 525nm. As predicted by figure 2.4, a non-smooth cosine function appears in the orange regime, between 575-660nm. The red regime (660-725nm) modulates properly, albeit with a different β. Naive filtering to isolate correct behaviour in a small optical bandwidth results in very low relative efficiency.

3

METAL-INSULATOR-METAL COLOUR FILTER

This chapter starts with specifying requirements for the enhanced ASP colours sensitive structure. The first step is to explore literature for candidate nanoscale colour filters. A Fabry Perot etalon structure, fabricated in nanoscale thin films, is an attractive candidate. The planar structure is fabricated and subject to measurement to extensively scrutinize suitability.

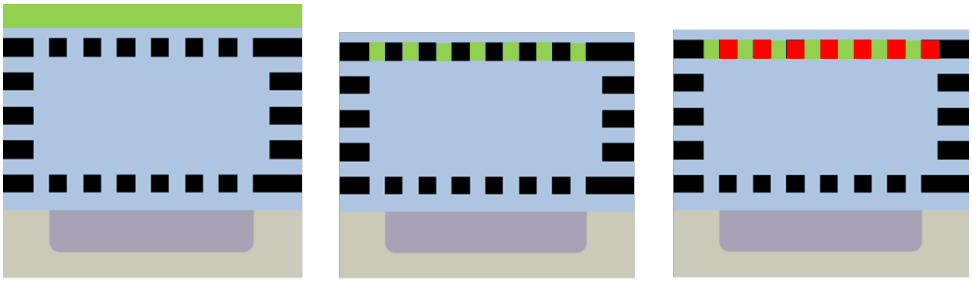

(a) Naive filtering method (b) Equivalent (c) Joint filtering

Figure 3.1: Thought process for redesigning ASP for colour filtering. The first naive approach is equal to a marginally thinner method of integrating filters inside the grating apertures. Observing that the talbot image is created by the blocking action of the amplitude grating, an ideal bandpass filter for another wavelength would have the same blocking thus diffracting effect. This second wavelength is diffracted similarly, hence a novel structure for dual wavelength diffraction is conceived.

3.1. REQUIREMENTS

Figure 3.1 shows the thought process for devising a colour filter interleaved grating. The requirements to this structure are as follows:

1. Smallest patternable feature size of $\lambda/2n$, in order to accomodate for all possible β.

2. No compromise in transmissivity thus SNR compared to current ASP solution

3. Keeping or improving all the tuneability properties as described in table 2.1

4. Be able to filter two arbitrary wavelengths in the visible spectrum with FWHM of (see figure 2.5).

The path for proving a structure as in figure 3.1c provides significant increase in performance will be done in five steps. First, implementation is described in sections 3.2 and 3.3. Second, it has to be proven that a dual talbot effect arises in section 4.2. Then, the ASP is finalized and measured in section 4.3. The last analysis, the limits of that ASP function is explored in section 4.4. It is crucial to be compared against previously constructed models to ensure predictability over a large tuning range. Finally, the device will be subject to comparative review in chapter 7.

3.2. CANDIDATES

Organic absorptive filters (figure 3.2a) are well-known [13] but not suitable for small scale integration due to bulkiness and possible chemical incompatibility. Nanohole array (figure 3.2b) [12,14] is promising in terms of requirements 2 and 3, but fails the first requirement as the spacing between each nanohole is already on the order of a few hundred nanometers. Patterning such a filter for blue light in glass ($\lambda/2n = 400/2{\cdot}1.5 = 133nm$) could be unreliable or even impossible.

The visually simplest solution of the three, the Fabry Perot is chosen for the following reasons. It is a planar stack in z, thus has patternable freedom in the x and y directions. The structure has a thickness on the order of a few hundred nanometers [15]. Transmissivity figures of 50% over the entire visible spectrum have been reported in that same paper. A practical argument is that the structure is relatively easy to fabricate, which makes the final product more attractive to the technology community.

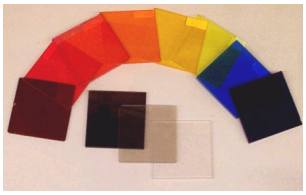

(a) Organic absorptive filters

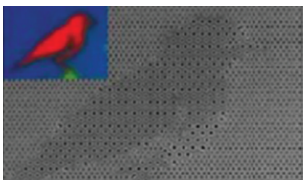

(b) Nanohole array [14]

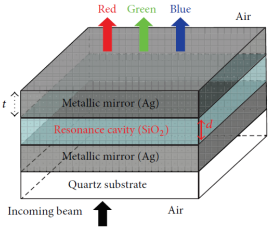

(c) Metal-insulator-metal Fabry Perot structure [16]

Figure 3.2: Three candidates for high q-factor transmissive optical bandpass filtering in the visible spectrum.

3.3. NANOPHOTONIC COLOUR FILTER BASED ON FABRY PEROT

Figure 3.3 illustrates the fabry perot interferometer principle and how this applies to a thin film implementation. The fabry perot cavity is constructed with two reflective materials (M), separated by a transparent material (I) with refractive index n. By selecting materials M that are partially reflective and partially transmissive, such as thin film metals [15], light can pass through. Each ray is partially contained, partially transmitted through, partially reflected back. When the optical path equals exactly an integer number of wavelengths, constructive interference occurs, and a transmission peak arises. The optical path, defined by the insulator thickness and refractive index, is stated in equation 3.1. Assuming no loss, the rest of the incident energy is reflected.

$$\lambda = 2nd\cos\theta \tag{3.1}$$

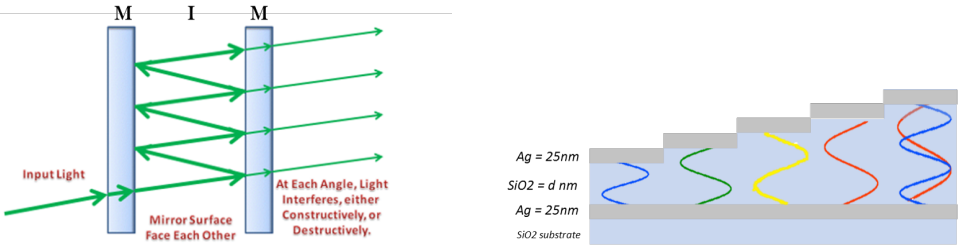

(a) Fabry perot principle

(b) Scaling of resonant wavelength

Figure 3.3: Fabry perot principle and its implementation as a thin metal film structure. By sweeping the separating dielectric thickness, the optical path length is varied and thus resulting in varying resonant mode.

3.3.1. FABRICATION AND MEASUREMENT

To verify claims made in [15] and to formulate cleanroom recipes, the Metal-insulator-metal structures illustrated before in figure 3.3b are fabricated and measured. For discussion on choices made in fabrication, challenges encountered, and the full recipe, refer to chapter 5. Figure 3.4a indeed verifies reliable bandpass filtering throughout the majority of the visible spectrum.

Measurement is done using a Hamamatsu UV-VIS spectrometer ranging well beyond the visible spectrum.

Equation 3.1 is reviewed and is regressed in equation 3.2.

$$\lambda = 2dn_{eff} \approx 2dn_{SiO2} \approx 3.3(d - 70nm) + 400nm \tag{3.2}$$

Even though efforts have been made to analytically derive the expression for the effective refractive index n_{eff} [17], this has only been done for electric field travelling through the insulator perpendicular as in a waveguide. A constant slope as in figure 3.4b leads to believe that for (small) changes in silver thickness, the effective refractive (as seen from the slope) index doesnt change, and thus almost exclusively depends on the insulator index.

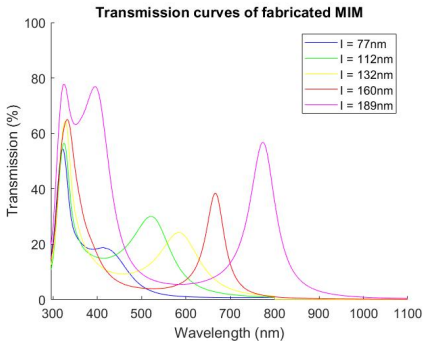

(a) Transmission spectra for MIM structures with 25nm Ag and different dielectric height.

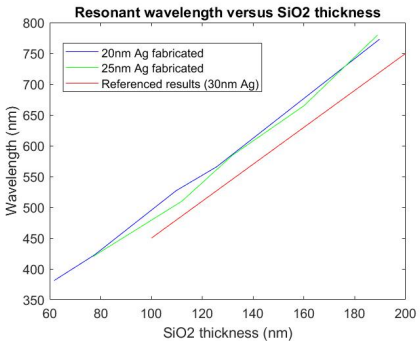

(b) All fabricated samples for two different Ag thicknesses and results from [15]

Figure 3.4: Measurement of planar MIM structures at normal incidence. Changes in peak transmissivity are due to fabrication imperfections. A very stable slope in resonance versus dielectric height is observed. The silver thickness was varied slightly to investigate the effect on resonant mode. No significant effect had been found. An approximatley same slope compared with the paper [15] is found. Offset from paper results, albeit small, are attributed to a completely different nanofabrication process.

3.3.2. MIM LIMITATIONS

The lower bound for robust MIM bandpass filtering is approximately 450nm. We see a constant transmissive peak at 330nm, manifested until approximately 400nm due to its limited q-factor. This transmissive peak is explained as its plasmonic resonance onset frequency [18]. In solid state physics from a photonic standpoint, metals are considered an electron gas. Those electrons have a metal specific resonance frequency, called the plasma frequency. Even though the plasma frequency is much higher than its onset frequency for interband transmissions [19], the latter already exhibits high transmissivity in a single layer of silver [20]. It should be clear that without reflectance, an FP cavity is not formed. Fortunately, this surface plasmon resonance at 330nm results in high reflectivity in the visible spectrum which will be further explained in section 5.2. The quick drop in transmissivity below 330nm is due to blocking of UV by the glass substrate.

The upper bound for robust MIM bandpass filtering is approximately 450nm. We see a half-wavelength, double frequency arises at λ=400nm in figure 3.4a for an insulator height of 190nm. This secondary resonance doesn't appear below the onset frequency for previously explained reasons.

Rotation Observant readers have noticed the angular dependency of the MIM resonance mode in equation 3.1. This effect is detrimental to the functioning of the ASP as it lowers transmission for a targeted constant wavelength when placed under an angle. Can a colour sensitive angular sensitive pixel even be constructed reliably if the angle itself changes the function?

This is a legitimate concern, and therefore the subject of verification by measurement.

Measurement is done with the setup in figure 4.10, and performed on a structure with resonant mode of λ= 620. Figure 3.5 presents the measurement versus simulation result. The effect is much less pronounced in the real device as opposed to simulation. The decrease predicted by theory and simulation is 150nm. The measured resonance decreases approximately 25 nanometers, well within the FWHM requirement. The decrease is also smaller than the wavelength separation required for correct functioning (figure 4.14), and thus poses no threat. Deposition nonuniformity produces a not perfectly smooth cavity. Incident waves see a complex structure whose resonant mode follows the interference equation but is less influenced by angle.

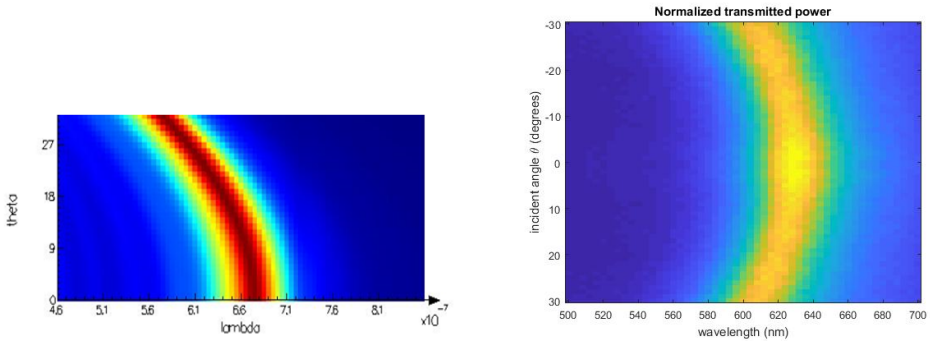

(a) FDTD simulation of MIM under rotation

(b) Measurement of MIM under rotation

Figure 3.5: Measurement and simulation of planar MIM structures (sample 3 in section 5.3). Angular limits are chosen according to (figure 4.11). A much less pronounced decrease in resonant mode, as compared to theory and simulation, alleviates the concern of infeasiblity as an ASP structure.

Loss in the MIM structure is a function of the silver thickness, assuming zero loss in the very thin SiO2. For bulk material, the extinction coefficient defines the loss in the material as a function of depth.

$$\eta = \exp^{-4\pi kz/\lambda} \tag{3.3}$$

However, for such thin materials that equation does not hold. The peak transmission is much higher than 1%, as predicted by 50nm of Ag in 3.3 at λ= 500nm. Thin film optical properties is the subject of a whole field of research, and as such the limit of choosing the metal thickness is not further investigated. It is hypothesized in literature that going thicker than 45nm is detrimental for transmission [15].

4

MIM GRATING

After having confirmed correct functioning of the candidate satisfying requirements, the grating structure is fabricated. Near-field scanning optical microscopy (NSOM) proves correct dual nonoverlapping talbot image generation. The ASP function is verified working. Finally, the limits in tuneability of the device are explored.

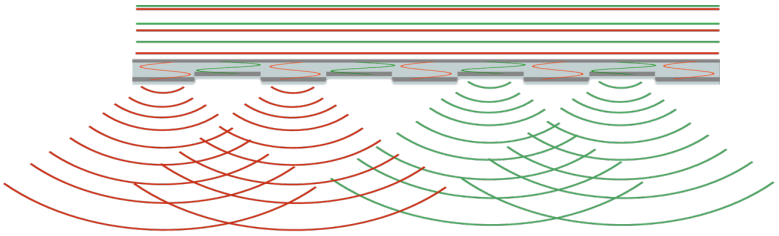

Figure 4.1: Prediction of creation of joint talbot effect by MIM grating. Lines are a phase height map, with each consecutive line a πphase distance, either constructively or destructively interfering with the same wavelength.

4.1. MIM GRATING TRANSMISSIVITY

The MIM structure is interleaved into a grating structure by etching (see chapter 5). A Scanning Electron Microscopy image of the is displayed in figure 4.2. The transmission curves of a combined MIM grating is shown in figure 4.3a. Figure 4.1 predicts generation of the two joint, independent talbot effects.

DISCUSSION ON MIM GRATING TRANSMISSIVITY

Two effects have notable influence on the cavity mode and/or transmission efficiency.

Secondary resonances There are two secondary resonances observed in figure 4.3. The first peak arises at exactly $\lambda = p/n = 700nm/1.5 = 460nm$ and as such is a lateral res-

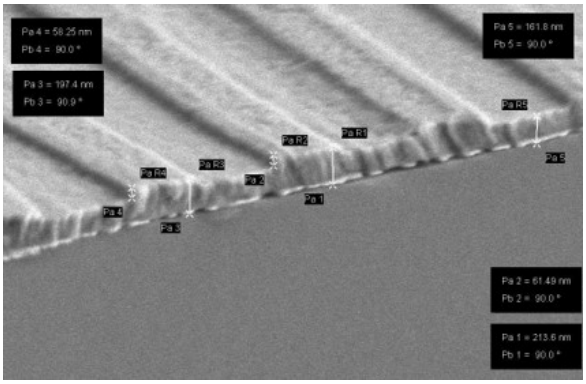

Figure 4.2: SEM image of the completed MIM grating with a pitch of 1µm. Approximate dimensions are displayed from SEM software. The sample was fabricated according to sample 1 in section 5.3, resulting in resonant wavelengths of respectively 660 and 450nm.

onance. The last peak at λ= 660nm is another lateral resonance as seen in FDTD simulation. Even though these wavelengths might be forming a (low intensity) talbot image, it was observed later on that these wavelengths are not modulated into an ASP function, and are therefore not harmful to the final functioning of the device.

Etch pitch size It is observed that the wavelength scales down from when the grating slit size becomes close to the wavelength size 4.3. For planar MIM, where the aspect ratio is infinite/very large, the cavity mode is calculated by simple Fabry Perot equations. By keeping the dielectric height constant and by decreasing the pitch, the resonant cavity aspect ratio decreases. This in turn decreases the effective cavity size and thus the resonant mode that fits inside the cavity. When the lateral cavity size approaches wavelength scale (i.e. the pitch approach 2 wavelength sizes), analytical modelling of the cavity mode is very difficult and should be extracted from numerical simulation and measurement.

Because the shift is properly predicted by simulation, it does not impede on the requirement of arbitrary wavelength filtering. The shift can be easily countered by increasing the dielectric thickness until the required resonance frequency is again achieved.

Polarization Figure 4.5 shows the effect of source polarization on both resonant wavelengths in the sample of figure 4.3. Measurement is done by fixing the device while inserting a polarization filter into a rotational stage (section 4.3). A photo of the setup is placed in appendix B. Measurement results are normalized to the peak transmissivity. Figures 4.5a and 4.5b both show that polarization parallel to the grating prefers the smaller cavity, while polarization perpendicular to the grating prefers the taller one.

Polarization influences the transmission efficiency in two ways. The efficiacy of the cavity mode differs per electric field components $[E_x, E_y, E_z]$ and therefore is a complicated

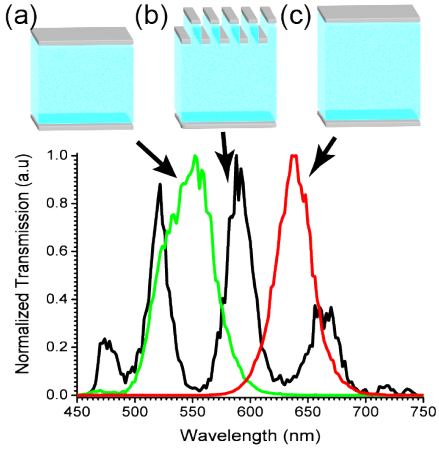

(a) Transmission figures of MIM interleaved grating (sample 3).

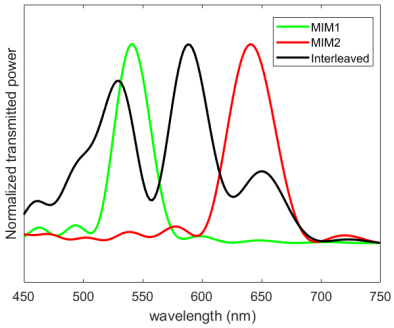

(b) FDTD simulation of transmission under circumstances matching measurement.

Figure 4.3: Interleaving the grating has the effect of superposing the two separate wavelengths. There is a slight decrease in resonant mode which is predicted by simulation. Two small lateral resonances appear, as predicted by simulation.

function of polarization. Secondly, by the wire grating analogy, polarization is inherently intensity modulated by the grating [21]. The structure has to be designed taking the source degree of polarization into account. All other measurements and simulations presented in this thesis are therefore performed using randomly polarized light, averaging out both effects. Again, simple simulations predict the effect, ensuring correct behaviour.

Duty cycle can be adjusted to increase transmissivity of one resonant wavelength over the other. This might be useful application specifically, where a larger number of sources of one wavelength is present in the scene. Due to its specificness, this is not further investigated.

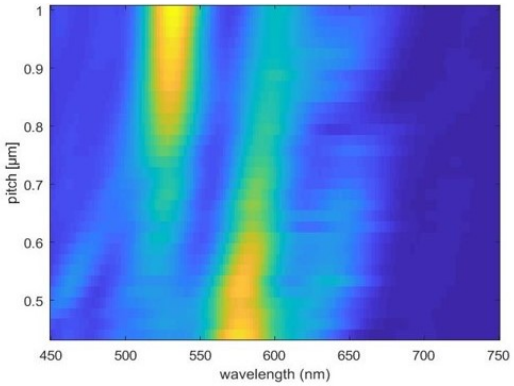

Figure 4.4: FDTD simulation of transmission under varying pitch for dimensions of sample 3 in section 5.3. A slight decrease can be seen, attributable to complex nanophotonic behaviour when the aspect ratio of the cavity decreases. Analytically deriving the behaviour of this decrease is omitted due to complexity. Pitch seems to prefer transmission of one mode over the other, choosing 0.7 µm as a tradeoff.

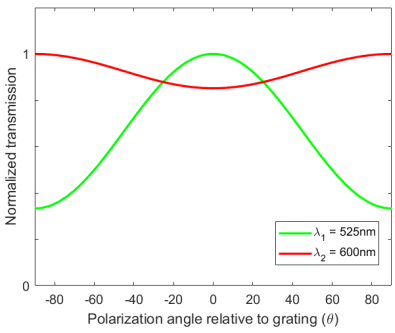

(a) FDTD simulation

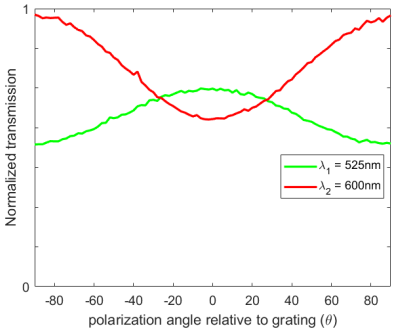

(b) Measurement

Figure 4.5: Polarization effect on the transmissivity of both resonant wavelengths.

4.2. DUAL TALBOT EFFECT FROM MIM GRATING

Having fabricated the grating, this section tries to prove the claims made in this section. There is a problem in validating the talbot effect. How is it possible to measure an electrical field with nanometer precision inside a volume? Not only are optical microscopes limited by the diffraction limit, they also record a far field projection, as the lens has to be placed exactly at the focal depth for sharp imaging.

The solution is to use Near-field Scanning Optical Microscope (NSOM) [22]. The concept is illustrated in figures 4.6 and 4.7.

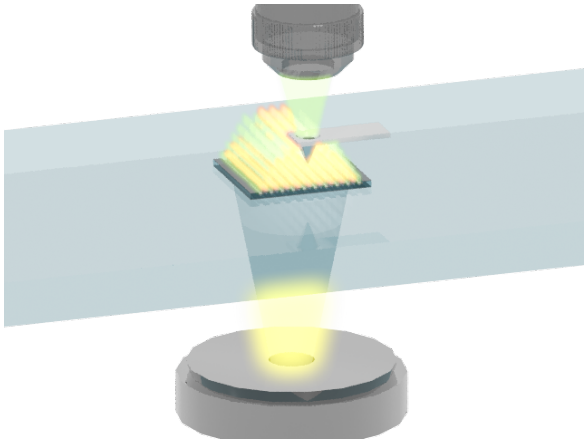

Figure 4.6: 3D illustration of NSOM measurement.

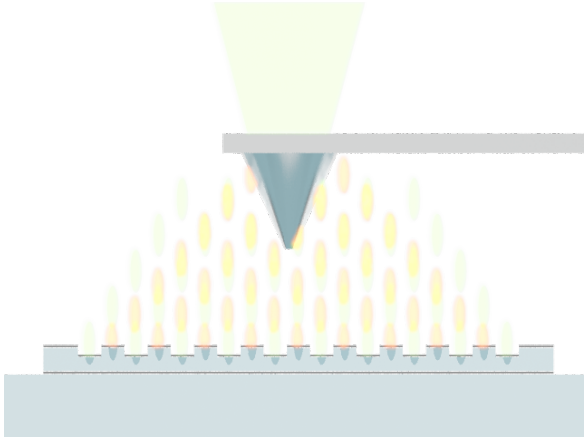

Figure 4.7: Sideview illustration of NSOM measurement.

The nanoscale near field Talbot measurement was done on a near-field scanning optical microscope (NSOM) equipped with two laser sources with wavelengths of 532 and

660 nanometers. The tool used was a NTMDT Ntegra system located at University of Pennsylvania, Philadelphia. The MIM periodic grating structure with multiple transmission peaks as depicted in figure 4.3a was used. An amplitude measurement was performed with the NSOM in transmission mode as depicted in figure 4.7. A cantilever with aperture of 70 ± 20nm was positioned at the MIM grating structure surface. The cantilever scanned the local light intensity, with lateral (ΔX, ΔY) resolutions of 22nm and vertical resolution (ΔZ) of 250nm. The electric field intensity in a volume of 4 µm cubed above the device was recorded.

The incident light was randomly polarized. Although polarization of the incident light can affect the coupling efficiency of generated Talbot image to the NSOM aperture [22] the two non-polarized laser sources yet we were able to measure the self-image as depicted in figure 4.8.

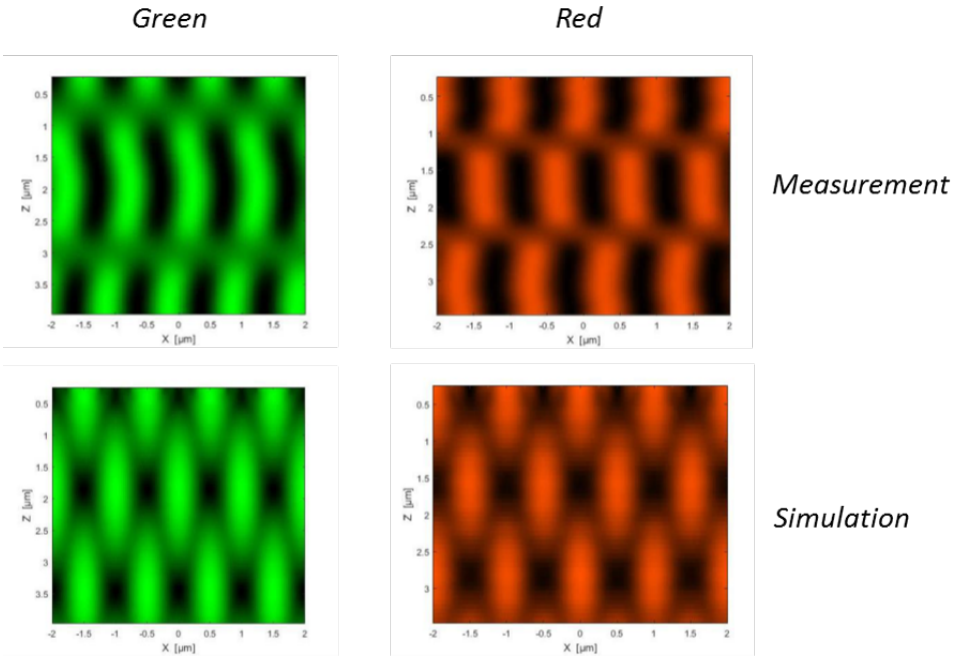

Figure 4.8: Talbot image measurement and simulation of the device depicted in figure 4.3a. By finding two non-overlapping talbot images, the novel effect of a colour filter-based diffraction grating is shown. The grating structure is located at the top of the image, with the substrate at z=0. Graph starts at 0.22 µm, the surface of the MIM grating structure.

The NSOM acquired (z-x) electrical field measurement is reconstructed with the extraction of the phase of the standing wave from measurement data. The displacement of the generated Talbot image at each z was modeled as sinusoidal function. The displacement was equivalent a Talbot phase shift across z direction. To clearly visualize the periodicity of the Talbot image we estimate the X-locations of maximum intensities using all available on multiple Y-slices (180 times). The Z-slices where a jump in intensity

location is detected define transitions to consecutive Talbot orders. The estimation is averaged over all Y-slices. Apart from removing measurement glitches, this method allows to cope with any rotation due to sample misalignment. Due to a mismatch between integer multiple of half Talbot depth and finite z resolution (250nm) of the NSOM measurement non-periodic measured intensity at irrelevant z position was omitted from the reconstruction. The first Talbot image was measured with half-wavelength offset relative to a traditional amplitude Talbot grating [7]. The half-wavelength offset is due to a fact that the first half wavelength is contained in the MIM structure itself, thus the shifted Talbot depth can be reformulated in equation 4.1.

$$Z_{T,k} = k\left[\frac{nd^2}{\lambda} - \frac{\lambda}{4n}\right] + \frac{\lambda}{2n} \tag{4.1}$$

4.2.1. TALBOT IMAGE DISCUSSION

The following observations can be made from the reconstructed talbot image in figure 4.8.

- The images of wavelengths 532nm and 660nm shows excellent agreement with equation 4.1 and FDTD simulation. The first Talbot orders are found at a depth of 2 µm and 1.7 µm for wavelengths of 532nm and 660nm respectively.
- The second order is verified at 3 µm in the red wavelength case. The periodicity for λ=532nm is found longer than predicted. This could be attributed to larger effective pitch size due to nonideal etching.
- Bending of the Talbot image in the 532nm measurement is attributed to drift in the tool.

Figure 4.9 shows the simulation result of the Talbot self-image rotates as the incident angle of light is shifted. Fabricating a secondary grating at this distance will produce a transmission curve modulated by incident angle. This secondary grating can be implemented for example as a blocking grating.

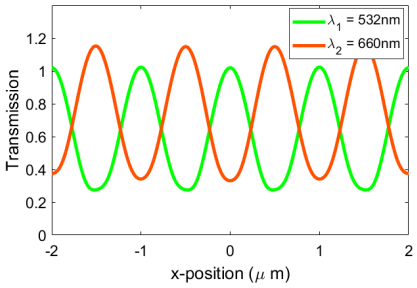

(a) Incident angle ϑ= 0 °

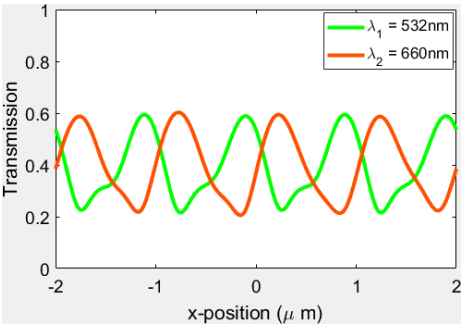

(b) Incident angle ϑ= 30 °

Figure 4.9: Slices of the FDTD simulated talbot image at z=1.7 µm, for two different incident angles. The value for z corresponds to the average of the two talbot distances at the first order. Fabricating a secondary grating at this distance will produce a transmission curve modulated by incident angle. The peak transmission at zero incidence is higher than unity, as the light is constructively interfered. The effect of rotation on transmission is clear in the rotated case.

4.3. MIM-ASP FUNCTION

After finishing the full ASP stack with a SiO2 grating separation and Chromium blocking analyzer grating (section 5), the device should be verified as ASP structure. For the measured sample, the pitch was chosen to be 0.7 µm and grating separation of 1.5 µm, placing the analyzer grating at the second talbot order.

4.3.1. MEASUREMENT SETUP

Measurement was performed according to figure 4.10. The tunable collimated light is generated by a wideband Xenon arc lamp, followed by a Spectral products cm110 monochromator SMA coupled to a Thorlabs fixed collimating lens optimized at 543 nanometers to be projected on to the ASP surface. The light is monochromated to separate the wavelength dependent and angle dependent effects.

Translational stages are used to finely place the device in the exact center of rotation. Finally, a Thorlabs P100d photodetector is fixed directly behind the sample, measuring the transmitted optical intensity. The angle is varied by mounting the sample and photodetector construction on top of a Thorlabs K10CR1 rotational stage.

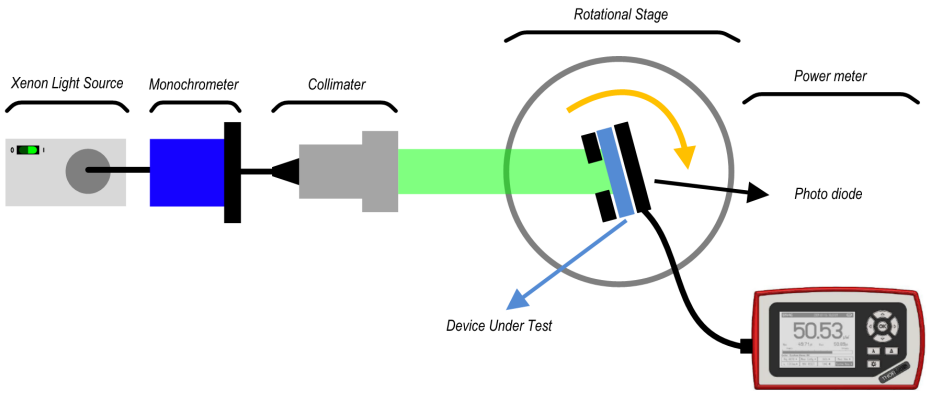

Figure 4.10: Measurement setup for measuring the ASP function. The measurement setup was designed to mimic a photodiode postprocessed with a MIM-ASP structure, sweeping the angle of incident light.

4.3.2. MEASUREMENT PARAMETERS

Adjusting the bandwidth is a tradeoff between incident optical signal power and spectral precision. We adjusted a slit size of the monochromator to achieve a bandwidth of 20nm. This allows for a high enough measurement SNR of 40 dB, and is still well within FWHM of a single MIM resonance filter as seen in figure 1. The latter point is important for separating the ASP functions of two spectrally close independent ASP functions.
The angular resolution of the measurement is set at 0.5 °. Finally, spherical aberration in the fixed collimator, stage uncertainty and reflections in the setup introduce measurement uncertainty. These error sources combined are designed to be below 0.1 °.

4.3.3. MEASUREMENT RESULTS

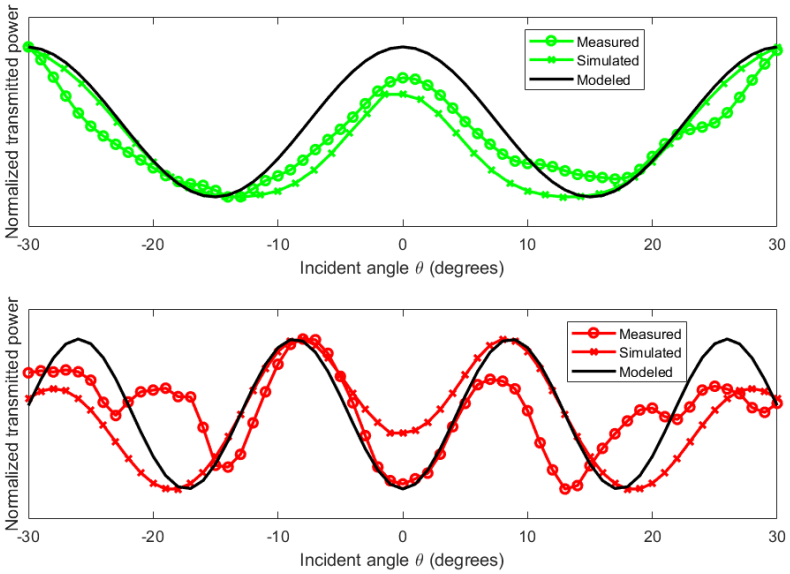

Figure 4.11: Measurement result for MIM-ASP structure for $\lambda_1 = 525nm$ and $\lambda_2 = 600nm$. Simulated efficiencies are 15% and 18% respectively. Simulated modulation index is 0.8, close to optimal. Measured transmission effciciencies are lower, on the order of 5%, while the modulation index is found to be 0.4.

Figure 4.11 compares the model, simulation result and measurement of fabricated device. The model is directly plotted with the measured data. The measured angular response is normalized to a baseline measurement of the photodetector with a fused silica substrate placed in front. To remove noise, the measured data was lowpass filtered with cutoff frequency one order of magnitude greater than β, and subsequently normalized. No shifting or other compensation was performed.

We see three direct results.

1. There is angle modulation for $\pm$ 30 degrees for both wavelengths.
2. The ASP functions of both wavelenghts are π out of phase with each other, showing again the correct formation of the nonoverlapping joint Talbot images.
3. Measurement data compares nicely to modeled and simulated data in terms of β. The device exhibits values for $\beta_{\lambda 1} = 12$ and $\beta_{\lambda 2} = 22$. This demonstrates that different values for β can be achieved for different wavelengths in the same structure.

These three findings prove the physical functioning of the proposed device.

Figure 4.12 defends the claim of transmission efficiencies on par with the metal ASP design [7].

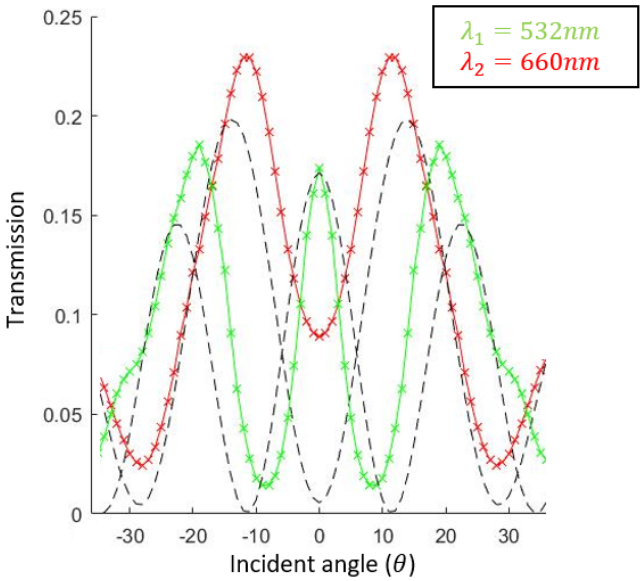

Figure 4.12: Simulation results with ideal maximally achievable transmission figures versus the model. The model is normalized to the simulation modulation index. The simulation is parameterized by device 2 in figure 5.2 with a metal analyzer grating at 1.65μm. Both red and green cases sport peak transmission of 18% and 22% respectively, and modulation indices of 0.8.

4.3.4. MIM-ASP DISCUSSION

To match the measurement, it was found that the grating separation had to be adjusted from the fabricated 1.7 µm to 1.9um. Four other differences with simulated results and the model are observed:

1. There are internal reflections in both cases (red at 19°, green at 22°). The reflectivity of the MIM silver layer and Chromium analyzer grating cause a multipath transmission to happen where a blocking should occur. This can be fixed by applying a high index antireflective coating such as Titanium Dioxide (TiO2) below the analyzer grating.

2. A slight deviation of the measurement result in beta compared to the model is noted. This is expected however from FDTD simulation in figure 4.13.

3. The non-symmetry in measurement of λ= 600nm can be attributed to a fabrication nonideality. After deposition of PECVD oxide as a grating separating layer, the etch pattern persists as a sinusoidal pattern in the PECVD oxide. This causes a slightly different path length for different incident angles, leading to higher angular frequency at positive incident angles than negative incident angles. This can be countered using Chemical Mechanical Polishing (CMP).

4. Because the Talbot distance shifts towards the grating with $Z = Z(\theta = 0)\cos\theta$, measurements done at incident angles at high incident angles (>30 °) have the secondary grating move out of optimality, severely affecting the modulation function. In standard CMOS processes, this maximum angle of incidence is furthermore limited by the aspect ratio of the metal stack height versus the photodiode width. The image is cropped to ± 30 to show correct operation in this useful regime.

5. Simulation shows peak transmission at any wavelength of 15%-20%, which is similar to peak transmission of an amplitude grating ASP. This is expected from a structure employing two consecutive structures blocking approximately 50% of the incident energy. Measured transmission efficiency is on the order of a few percent, as opposed to 15% in simulation. This efficiency is largely dependent on nanofabrication quality and moving towards this ideal case is therefore subject of a further research.

4.4. MIM-ASP TUNEABILITY

Now we have satisfied the first two requirements of section 3.1, the requirements on freedom of tuneability are explored. Because these involve large sweeps, FDTD is employed rather than nanofabrication.

β-TUNEABILITY

Figure 2.3 is reproduced for the MIM-ASP structure in figure 4.13 using the same FDTD simulation setup. Only the grating separation is decreased to 3.8µm, the numerical average of the two talbot distances at the fourth order according to equation 4.1. It shows excellent agreement with theory as in table 2.1.

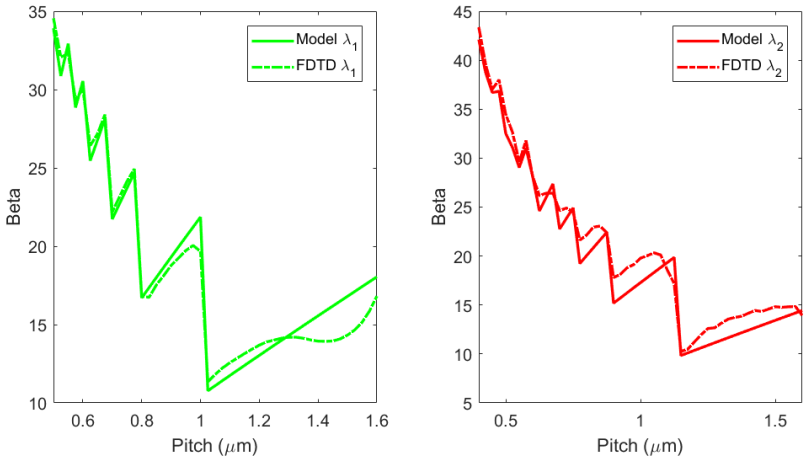

Figure 4.13: FDTD simulation showing tuning of angular frequency β by adjusting pitch (**p**). $\lambda_1 = 525nm$, $\lambda_2 = 600nm$. The grating separation is placed at 3.8µm, the numerical average of the two talbot distances at the fourth order according to equation 4.1. Even though the talbot grating is not at optimal distance for all combinations of pitch (**p**) and λ, the model is respected over a large range of pitch sizes.

WAVELENGTH SEPARATION

The last specification requires an arbitrary choice of two wavelengths to be filtered. Figure 4.14 shows an FDTD simulation where one wavelength is held constant at around 575nm (center of visible spectrum) by a thickness of 170nm. The etch depth is swept as to change the primary wavelength. The pitch is equal to to mimic the device in 4.3. A minimum height difference of 30nm should be attained to distinguish two wavelengths with full modulation depth. Below that minimum separation, the grating effect disappears and the structure behaves as a planar MIM.

The resulting wavelength separation in shown in figure 4.14b. This analysis on idealized simulation shows that using two arbitrary wavelengths as spectrally close as 50nm can be distinguished using the MIM-ASP structure. The measured device (done previously in (figure 4.11) with an etch depth of 35nm is indeed verified by simulation to be

able to achieve closer wavelength separation than the Fabry-Perot predicted wavelength separation (equation 3.1). The pitch is 700nm, sizing the width of a single cavity around the wavelength scale. For small wavelength separations, there is an observed interdependence between the two resonant modes. Again, a complex expression for the cavity mode causes this nonlinear effect.

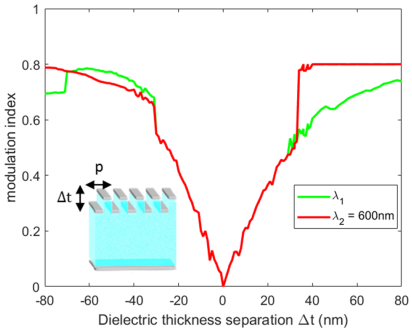

(a) FDTD simulation of modulation index under dielectric thickness separation.

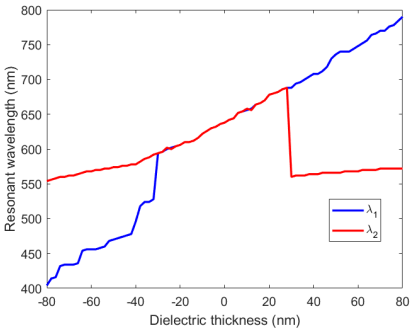

(b) FDTD simulation of resonant wavelengths under dielectric thickness separation.

Figure 4.14: The dielectric thickness Δt for λ_2 is held constant at 170nm. λ_1 varies between 400 and 800 nanometers. Two distinct resonant wavelengths are observed until the grating effectively dissapears at Δt = 30nm. A constant high modulation index of 0.8 is observed until the grating effectively dissapears at Δt = 30nm. The smallest observed wavelength separation is approximately 75nm.

5

FABRICATION OF THE MIM-ASP DEVICE

Interfacing circuits to real life using custom postprocessing schemes is where the cutting edge lies for many subdisciplines in microelectronics. This chapter briefly illustrates the steps required for nanofabrication of the MIM ASP structure. Some challenges, previously unknown to a student electrical engineering, related to chemistry and materials sciences are highlighted.

5.1. COMPLETE RECIPE

The following recipe is designed from scratch to produce the MIM2D + analyzer grating. Challenges leading to choice of the subrecipies are described in section 5.4. All nanofabrication was performed at the Advanced Science Research Center at the City University of New York.

1. Piranha clean 2" fused silica wafer
2. RF magnetron sputter 15 nm SiO2 @ 200°C as a buffer 'adhesion' layer
3. DC magnetron sputter 25 nm Ag @200°C, RF Sputter 170nm of SiO2 @ 200°C
4. E-beam lithography 350nm wide lines in 300nm high PMMA 495 A6 ($400^{uC}/_{cm^2}$)
5. Develop for 60 sec MIBK-IPA 1:1, stop IPA, medium-bake the PMMA for 1 minute @100°C
6. Etch the SiO2 for 35nm in the 1:1 CHF3/Ar mixture at 100W
7. Strip PMMA using consecutive RPG, Acetone, IPA baths
8. DC magnetron sputter 25 nm Ag @200°C, RF Sputter 20nm of SiO2 @ 200°C to block oxidation

9. Create the SiO2 grating separation of Z_T=1.5µm using PECVD @200°C
10. E-beam lithography 350nm wide lines in 300nm high PMMA 495 A6 ($400\mu C/cm^2$)
11. Deposit Cr for 100nm, liftoff the pattern to create the analyzer grating
12. Passivate the device with 3µm PECVD oxide @200°C

5.2. CHOICE OF MATERIALS

Even though [15] and [7] use specific materials which can be mirrored, the choice should be subject to critical review. At first it should be questioned what material is useful for MIM Fabry-Perot cavity. The candidates are summarized in table 5.1.

Table 5.1: Tabulation of available materials for nanofabrication at CUNY-ASRC cleanroom

	Metal [Ag]	**Insulator [SiO2]**	**Analyzer grating [Cr]**
Requirements	Low extinction coefficient possible Reflectivity over full visible spectrum	Deposition without breaking vacuum	High reflectivity to minimize losses Good adhesion to the grating separating insulator Ease of liftoff
Available candidates	Noble metals Transition metals Aluminum	SiO2 Hafnia [HfO2] Alumina [Al2O3]	Noble metals Transition metals Aluminum

The grating separating material was automatically chosen equal to the MIM-insulator to remove any refractive effects. SiO2 is the only material that was available for nanometer scale (RF magnetron sputter) and micrometer scale (PECVD) deposition methods, and was chosen as such.

MIM materials Noble metals are frequently used in nanophotonics because of their ability to excite surface plasmons at visible frequencies [23]. Figure 5.1 shows the transmission spectra of the three cleanroom available noble metals (excluding Platinum and Palladium). Thin (25nm) films of Ag, Au and Cu are respectively deep blue, green and yellow coloured. Wavelengths above these onset plasma resonances are reflected. Ag is therefore useful candidate for spanning the entire visible spectrum.

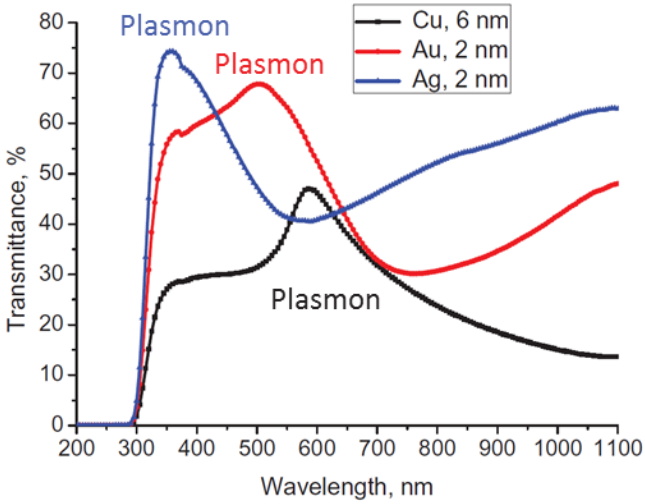

Figure 5.1: Transmission spectra of noble metals Ag, Au and Cu in the visible spectrum. Due to interband transitions, gold and copper do not reflect over the entire visible spectrum.

Platinum and Palladium have behaviour similar to silver [24], although with a slightly higher extinction coefficient, and having the drawback of being much more expensive. They are available for evaporation, but not for sputter (see section 5.4). Price is not a relevant argument in research, but it is in large scale commercial integration (figure 1.2).

Analyzer grating materials Pt and Pd, being good reflectors throughout the entire visible spectrum, are not useful for patterning the analyzer grating, as they are too expensive. Ag does exhibit plasmonic surface resonances at frequencies of interest which could couple to the waves passing through the grating, forming an undesired spectral filtering [35]. Decent reflectivity is found in transition metals such as Titanium and Chromium, or in Aluminum. All three have good adhesion to glass, but Chromium is experienced as easier to liftoff due to its softness. Liftoff is preferred to etching as it is extremely easy with PMMA. Aluminum was the first choice due to its higher reflectivity, but was not available anymore at the time of the final device fabrication.

5.3. FABRICATED DEVICES

In chapters 3 and 4 a number of figures were presented showing results from three different devices. Table 5.2 clarifies the exact structure belonging to each figure.

Table 5.2: Tabulation of fabricated and simulated device dimensions. Only MIM grating and MIM-ASP devices are tabulated.

Used in	**Figures 4.2**	**Figures 4.8, 4.9**	**Figures 3.5b, 4.3, 4.4, 4.5**	**Figures 4.11, 4.13, 4.14**
Dimension	Sample 1	Sample 2	Sample 3	Sample 4
Ag height	25 nm	25 nm	25nm	25nm
SiO2 height 1	100nm	140 nm	135nm	135nm
SiO2 height 2	160nm	180 nm	170nm	170nm
Pitch	1 µm	1 µm	0.7 µm	0.7 µm
Grating separation	N/A	N/A	N/A	1.7 µm
Analyzer grating height	N/A	N/A	N/A	100 nm
Oxide passivation height	N/A	N/A	N/A	3 µm

5.4. CHALLENGES

This section highlights four interesting cases having challenged my nanofabrication efforts. For conciseness, not every decision is documented.

5.4.1. IMPROVING E-BEAM LITHOGRAPHY WRITING TIMES

Wavelength-scale feature sizes are in a suboptimal regime for both photolithography and electron beam lithography. Missing a wafer stepper, the available photolithography tool was the EVG620 Mask Aligner. As such the minimum feature sizes are limited to approximately 2 µm. At the same time, detector sized area's of several square millimeter should be fabricated to have decent signal strength at the measurement setup's photodiode. For those area's, electron beam lithography becomes expensive. A sensitive resist, requiring a low dose, should be chosen. PMMA is a versatile resist, having good adhesion and liftoff properties. Even though it reflows above 120°C, it can be used as an etch mask by keeping etching power low. The true beauty of PMMA is its range of sensitivity and resolution by chosing the proper developer [25]. By switching from IPA/H2O 3:1 to a much stronger solvent, MIBK:IPA 1:1, writing times have been reduced by a factor 2.5. Sensitivity is a tradeoff with resolution, which can easily be made for the feature size of a few hundred nanometers.

5.4.2. REDOX REACTION

Sputtering of SiO2 at a higher temperature leads to a denser material, with improved optical properties [26]. The standard optimized SiO2 PECVD recipes are also performed at 350°C. This led to the result in figure 5.2. The following reaction takes place:

$$SiO_2 + 4Ag \xrightarrow{250\,°C} Si + 2Ag_2O$$

This can be seen by the blue/green colour, indicative of oxide on silicon, and a brownish colour, indicative of silver oxide. Silver has a slightly higher electronnegativity than Silicon ($\Delta\xi$= 0.03), causing the exchange of oxygen. The temperature must then be lowered, but kept as high as possible to guarantee high quality oxide films. The temperature was stepped down, and eventually the tradeoff was made by performing sputtering and PECVD at 200 °C, where the reaction dissapeared.

5.4.3. DELAMINATION

Bad adhesion is an often recurring problem in nanofabrication, as shown in figure 5.3. It is primarily caused by the mismatch in atomic structure of the two materials. The problem is amplified by mismatch of residual stress in the silver film [27,28]. The smoothness of the fused silica is 'too perfect'. A common adhesion promoting method is to evaporate a few nm of Chromium right before evaporating silver. This method was tried on the device in 5.2 without succes. The Chromium didnt cover the entire wafer, as can be seen from delamination above the square patterns. Deposition of more chromium is harmful to optical properties. A solution is to change deposition method to magnetron sputtering [29]. The residual stress can be matched to the SiO2 by keeping a constant high temperature while switching depositions. Before silver deposition, a thin (15nm) layer SiO2 is

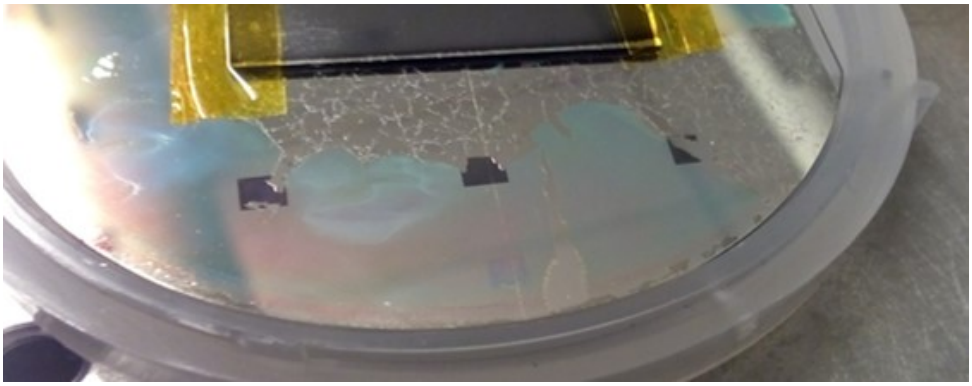

Figure 5.2: Redox reaction between SiO2 and Ag at elevated temperatures on the recipe of sample 4.

Figure 5.3: Delamination after attempting to dice the wafer into separate devices. Adhesion between glass and silver films is a difficult issue, and is solved by DC magnetron sputtering the silver.

deposited. This creates some surface roughness. Lastly, the sputtered atoms penetrate the underlying SiO2 layer for a few angstrom due to the high energy of sputtered atoms, creating an intermingling layer. The sputtering solution completely solved the issue.

6

NEAR FIELD IMAGING USING MIM-ASP

Near-field imaging is a very interesting application for lensless imaging. In this thesis, near field image is defined as the volume with vertices on the order of the sensor width. This chapter presents a simple simulation that illustrates how the MIM-ASP should outperform previous ASP structure in a multichromatic scene. Both stability in response and the joint wavelength decoding lead to this hypothesised result.

A biomedical application of lensless imaging will be illustrated in this chapter. In neural imaging, sources of interest (fluorophores) are sized on the order of several micrometer [30]. A future goal is to make an implantable device, placing the detector surface very close to the neural tissue. This makes neural imaging almost impossible for lensbased imaging.

6.1. SIMULATION SETUP

Consider the scene of figure 6.1 [31]. Two different fluorophores are inserted, both are an indicator of different biological activity. Building imaging sensors for neural systems is a core line of research for the Bioelectronics Systems Lab, hence the selection of such a scene as the example.

Transmission efficiencies of both ASP and MIM-ASP are taken equal for any wavelength. The modulation index is taken as 0.4 for the ASP [7] and 0.4 for the MIM-ASP 4.9.

All sources have unity intensity. Assuming fully isotropic sources, the signal intensity scales inversely by the radius squared. The noise variance on the detector is equal over all detectors and is calculated by equation 2.3. Signal strength σ_s is defined as the average received intensity over the detectors.

To illustrate the example better, the problem is reduced to a two dimensional setup, in X and Z. The area to be reconstructed is 5mm wide and 2mm high. The area is discretized

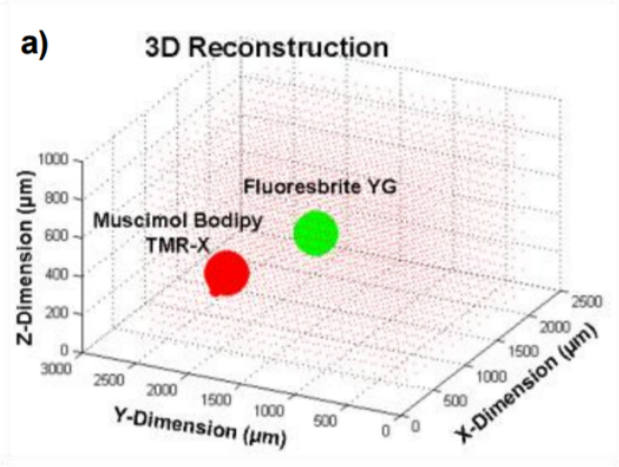

Figure 6.1: 2D illustration of a near-field biological imaging scenario. The Fluoresbrite YG bead has an emission of 486nm [32], the Bodipy TMR-X emits at 574nm [33]. These are separated spectrally far enough for the MIM-ASP to function correctly.

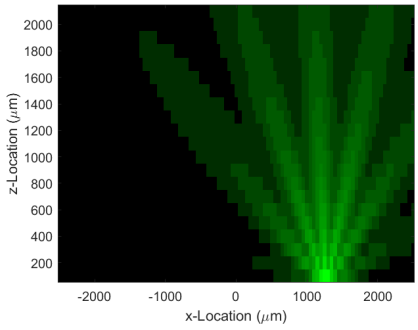

(a) Green wavelength response. $\beta = 14$, $\alpha = \pi/3$, $m = 0.4$

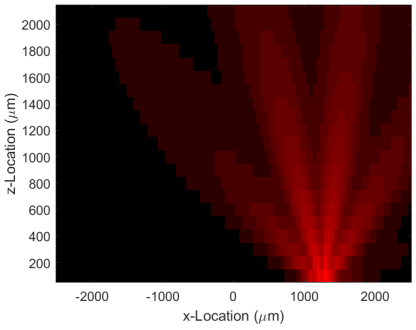

(b) Orange wavelength response $\beta = 10$, $\alpha = 4\pi/3$, $m = 0.4$

Figure 6.2: Spatial response of the MIM-ASP inside the area of interest for both green and red wavelengths. The detector is picked randomly from the array and has offset of . Even though the same detector will pick up signal from different sources, it will be demonstrated that this method is very benificial for reconstructive ability.

in ΔX = 50 µm by ΔZ = 100 µm. All detectors are placed with linear spacing fully spanning the X-axis at Z = 200um 0. The detectors are laid out in linearly increasing β from 10 to 35 (figure 4.13). To fully cover the area of interest with response from each β, three detectors with three different phases $\alpha[\pi/3, \pi, -\pi/3]$ are placed per β. This three-phase sensing guarantees constant intensity over the scene from each angle [31].

A deadangle is incorporated by multiplication of the sinusoidal response with a cosine window. The result of a single MIM-ASP detector in the set is visualized in figure 6.2 for both wavelengths. The complete response is reformulated in equation 6.1.

$$I_{tot} = I(\theta) * \text{deadangle window} * \text{isotropic decay}$$
$$I_{tot} = \left[1 + m\cos\left(\beta\theta + \alpha\right)\right]\cos(\theta)\frac{1}{r^2} \tag{6.1}$$

Because of the deadangle, in order to have each point in space covered by each β again, the range of β is linearly interpolated four times, thus implementing each β four times for each of the three phases (#detectors=12#β). A total number of 264 detectors are thus placed on a line of 5mm, which is generously sized to have enough grating periods per detector.

6.2. RECONSTRUCTION METHOD

Each ASP has a defined spatial maping from each point in space to the detector. The individual spatial responses are combined into the array response matrix **A**. Combining these mappings over multiple ASP's does not place every source on a unique detector. Instead, the mapping is different for every ASP, creating reconstructive ability.

6.2.1. AMPLITUDE GRATING ASP MONOCHROMATIC SCENARIO

The detector response vector **Y** is created by multiplying the response matrix **A** with the source intensity vector **X**, as in equation 6.2. **X** is a vector with number of elements the amount of discretizations of the area to reconstruct, in which only the source locations are have unity value, and others zero. Noise is added according to equation 2.3.

$$Y = AX + n = AX + \mathcal{N}(0, \sigma_n^2) \tag{6.2}$$
$$A = U\Sigma V^H \tag{6.3}$$
$$\hat{X} = V_A\Sigma_A^{-1}U_A^H Y \tag{6.4}$$

The quality of reconstruction is quantified by the singular values (elements of Σ in equation 6.3) of the combined response matrix **A**. These singular values are plotted in figure 6.3a. Singular values with large magnitude carry information, singular values with small magnitude carry no information. In a detector setup with perfect spatial discrimination, the singular values would show constant high magnitude without sudden sharp decline. Figure 6.3a shows that for this detector setup, the first approximately 200 singular values carry have relatively good magnitude. The rest should be discarded as they

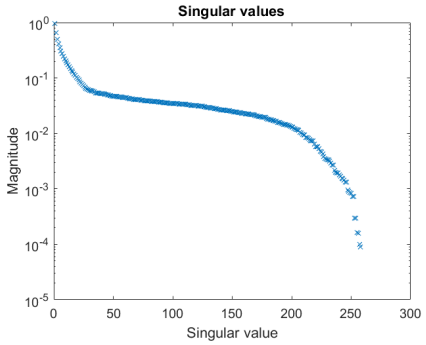

(a) Singular values for A-matrix of ASP, condition number = 1120.

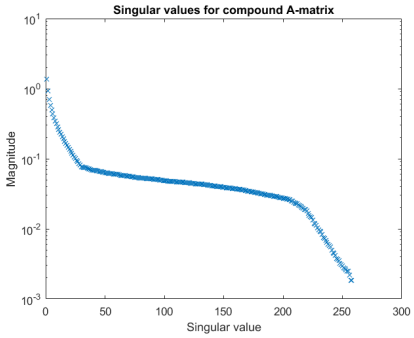

(b) Singular values for compound A-matrix of MIM-ASP, condition number = 760.

Figure 6.3: Singular values for the matrices constructed for the detector arrays of section 6.1. The approximately 200 first singular values are high enough in magnitude to carry information. In noisier scenario's, more singular values can be rejected to tradeoff information for noise rejection. The condition number is lowered by a factor 0.65 for the MIM-ASP compound A-matrix. This implies better noise rejection capabilities, because of less susceptibility to disturbances. Still, the roll-off happens at the same SV number. This implies that the spatial/numerical beta-layout is the decisive factor for the rank.

will amplify noise in the reconstruction. This is quantified in the condition number in equation 6.5. A lower condition number gives lower susceptibility of the output to a disturbance (noise).

$$cond = \frac{\sigma_{max}(A)}{\sigma_{min}(A)} \tag{6.5}$$

To optimize the singular values in the A-matrix further, the combination of β, α and their locations can be optimized. This is outside the scope of this demonstration.

6.2.2. AMPLITUDE GRATING ASP DICHROMATIC SCENARIO

The scenario deals with two distinct wavelengths, causing distortion in the detector response. Looking back to figure 2.5, β deviates between some bounds. Although we can measure this response, the source wavelength is uncertain, therefore β should be modeled with uncertainty. In order to take this uncertainty into account, the detector response is constructed using a matrix **B** with uncertain β (equation 6.6).

$$\beta \Rightarrow \beta + \mathcal{N}(0, \sigma_\beta) \tag{6.6}$$

$$Y = BX + n \tag{6.7}$$

$$\hat{B} = A \tag{6.8}$$

$$A = U\Sigma V^H \tag{6.9}$$

$$\hat{X} = V\Sigma^{-1}U^H Y \tag{6.10}$$

As we can only use what we know, reconstruction has to be performed using the **A**-matrix as in equation 6.10. Because **B** is modeled gaussian, **A** is the best estimator for **B**

in equations 6.8 to 6.10.

6.2.3. MIM ASP UNDER DICHROMATIC SCENARIO

Lets take a closer look at the reconstruction equations for the MIM-ASP. The thesis states that the MIM has two distinct out of phase responses for the two wavelengths. Unlike the ASP, the responses are perfectly known and stable under wavelength shift. Source wavelengths within close to the resonance frequencies are modulated, other wavelengths are rejected by filtering. This implies that we can expand the linear equations to a system of the form in equation 6.11.

$$Y = \begin{bmatrix} A_G & A_R \end{bmatrix} \begin{bmatrix} X_G \\ X_R \end{bmatrix} + n \tag{6.11}$$

$$\hat{X_G} = V_G \Sigma_G^{-1} U_G^H Y \tag{6.12}$$

$$\hat{X_R} = V_R \Sigma_R^{-1} U_R^H Y \tag{6.13}$$

The rank of the compound **A**-matrix does not increase as its row space is not increased. The singular values show only marginally better behaviour as seen from the condition number in figure 6.3b. It is not a two-fold increase in information extraction. However, the reconstruction quality is highly increased for the following two reasons:

1. The problem is separable into reconstruction for green and red. This holds because the matrix $\mathbf{A}_\mathrm{G}$ differs from matrix $\mathbf{A_R}$. Their individual responses are not only out of phase, but are also parameterized by different values for β. This alone removes the uncertainty introduced in equation 6.10 and brings the reconstruction back to the quality of equation 6.4.

2. Classification can perform much higher. If the scene is sparse, two fluorophores will not be closely located to each other. A joint iterative classification can be set up where the classified location of one type of fluorophore can be used as a priori information for reconstructing locations of the other type. In other words, the location of type 1 fluorophore can be excluded as possible locations for type 2, enhancing the prediction.

6.3. RECONSTRUCTION RESULTS

For each simulation, the SNR is decreased from 1000 downto 1. The reconstructed image is visually inspected, and the amount of rejected singular values is varied manually to scout for possible improvement in each case. The original scene is plotted next to each simulated experiment. Circles are placed manually at locations with high probability to be picked out by a detection algorithm. The classification accuracy is defined as the percentage of correctly localized fluorophore locations. This detection and localization however is the of a whole new field of study and therefore not investigated.

ASP RESULT MONCHROMATIC SCENARIO

Figure 6.4 shows the first experiment. It is setup according to section 6.1 and reconstructed using equations 6.2 until 6.4.

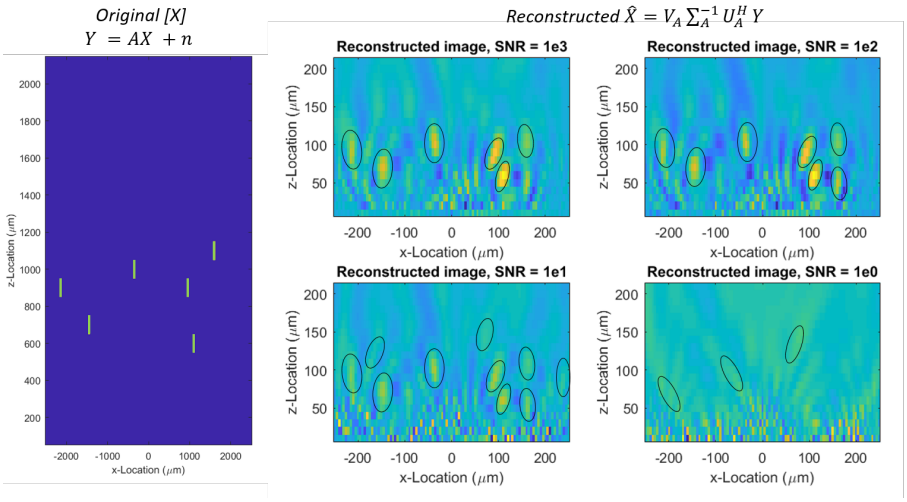

Figure 6.4: Reconstruction for the scenario of completely certain ASP response. The most probable locations are manually highlighted. For low noise, reconstruction can distinguish the fluorophore locations with high certainty. It is observed that ability of localization dimishes gradually with decreasing SNR. For SNR = 100, the true locations appear dimmer such that more false potential locations arise. This trend progresses until no real high probability locations are found anymore for SNR = 1.

ASP RESULT DICHROMATIC SCENARIO

Figure 6.4 shows the second experiment. It is setup according to section 6.1 and reconstructed using equations 6.6 until 6.10.

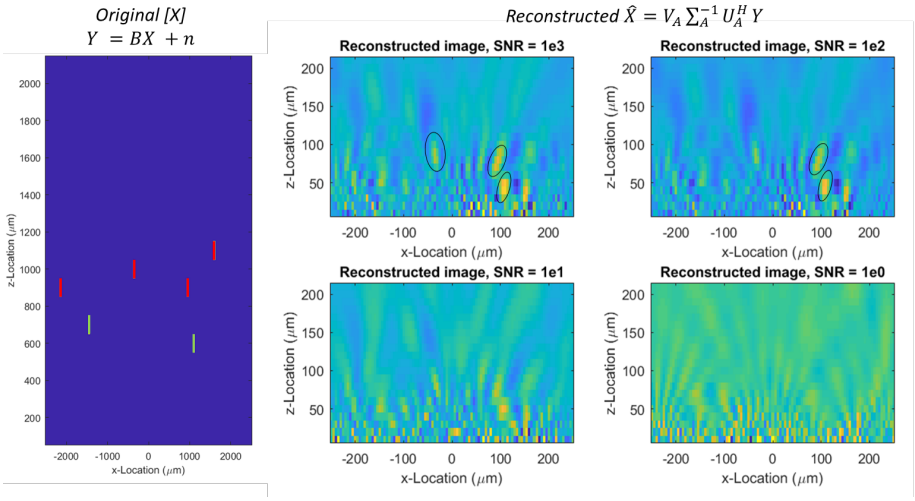

Figure 6.5: Reconstruction for the scenario of uncertain ASP response due to multicolored nature of the scene. The most probable locations are manually highlighted. Even for low noise, only a few fluorophore locations can be distinguished with high probability. Decreasing the SNR has a negative effect, but clearly distortion overshadows the noise, and as such, causes a sharp decline in reconstruction accuracy compared to figure 6.4.

MIM-ASP RESULT DICHROMATIC SCENARIO

Figure 6.4 shows the third experiment. It is setup according to section 6.1 and reconstructed using equations 6.11 until 6.13.

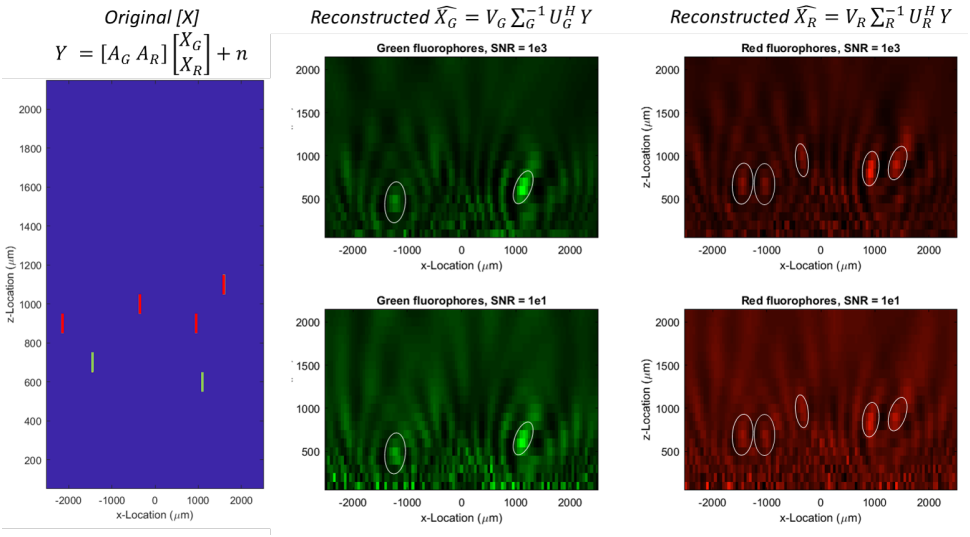

Figure 6.6: Reconstruction for the scenario of MIM-ASP response and separated reconstruction. Four observations are made. Firstly, the green fluorophores can be almost perfectly localized. The noise does not seem to have any effect for green fluorophore localization, not even by jumping two orders of magnitude. Secondly, the red reconstruction can localize three out of four correctly, and places two fluorophores at the left-hand side green location. Thirdly, only the farmost left-hand side red fluorophore is not showing clearly at all. Lastly, by implementing a classification algorithm that implements sparsity, the two red locations on the left can be rejected. This would leave the image reconstructed with five correct fluorophores, zero false classifications, and one fluorophore lost.

6.4. IMAGE RECONSTRUCTION DISCUSSION

The computational imaging is barely touched upon in this thesis, and is the subject of a whole new line of research. To start off, a using just a simple pseudoinverse is not optimal. This is because of several edge cases:

- When the fluorophore is extremely close to a detector, it will immediately saturate just that detector, while not exciting other detectors. That means the reconstruction will be distorted. A solution for this will be to detect a fluorophore there, and remove the detector from the set of equations.
- Due to the deadangle, MIM-ASP will have very low signal strength at high incident angles. The least squares solution nevertheless tries to reconstruct for these angles, essentially amplifying a lot of noise.
- The simulation was done in a small restricted volume assuming no correlated

sources caused by reflections, refraction etc. This should be modeled according to the application.

7

ASP COMPARISON AND DISCUSSION

This chapter starts by concluding the results on the MIM-ASP research. It continues by comparing results with the existing ASP method and further discuss advantages and drawbacks. Being inspired by other implementations of monochromatic ASP, the MIM-ASP can be further improved.

COMPARISON

Figure 7.1c shows an interpretation of CMOS-implementation of the proposed device alongside illustrations of the existing ASP methods. The phase grating method [7] improves transmission efficiency by a factor of 2 as it increases the transmissive surface area by 2. The diffraction effect is formed by the optical path length difference between the insulator and air, equalling half a wavelength. Excluding the phase grating from this comparison would be unfair, as it shows other paths of improvement for ASP for monochromatic scenes. A few other optimizations for ASP are presented in [7], but as they make assumptions on the technology node, they are not shown.

The advantages and drawbacks of all three structures are discussed in table 7.1.

DISCUSSION

The amplitude + analyzer ASP has the major advantage of having the possibility to be implemented in CMOS by the interconnect wiring. It can be designed from the IC CAD tool without any expensive and time consuming postprocessing steps. Exactly this fact will let the method stay attractive for many proofs of concepts in lensless imaging, if SNR is not the main concern.

For monochromatic scenes, the phase grating remains a better option due to its high transmission efficiency. It is still relatively easy to postprocess. The pitfall with the phase grating is its inherent incompatibility with any kind of colour filter. It relies on a refractive index difference. As a filter cannot float on air, a solid with a relatively high or relatively

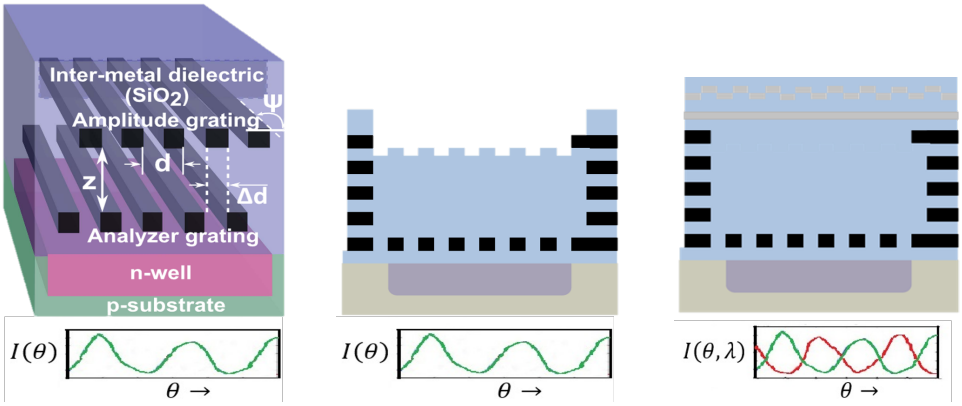

(a) Amplitude grating ASP. (b) Phase grating ASP. (c) MIM grating ASP.

Figure 7.1: Comparison of Amplitude + analyzer ASP, Phase grating + analyzer ASP [7], MIM grating + analyzer ASP. The common denominator of these three structures is zero assumptions on the underlying technology node. These structures can be implemented in any nanophotonic application, or integrated as part of a more complicated structure.

low index (compared to glass) should be deposited, adding complexity. The colour filter can be postprocessed underneath, but that clearly defeats the argument of easy post-processing. Equipping the phase grating structure with a planar colour filter brings the efficiency on par with the MIM-ASP, but for only a single wavelength.

The MIM-ASP structure definitely adds steep postprocessing requirements, the most important of which is the use of silver, which is not standardized in CMOS processes. When imaging dichromatic scenes however, his thesis proposes that the MIM-ASP is a very large step forward in overall reconstructive ability. Instead of equipping each pixel with a colour filter in RGGB tiling, an array of [RG] and [GB] pixels can be designed, doubling the effective number of pixels. This is without diminishing signal intensity compared to the amplitude + analyzer ASP.

Furthermore, chapter 9 will present some ideas to get the transmission efficiency up to the level of the phase grating.

Table 7.1: Tabulation of advantages and disadvantages of the three structures depicted in figure 7.1. Transmission values are average transmission percentages. All structures achieve a modulation index of 0.8.

	Metal Amplitude and Analyzer	**Phase grating, metal analyzer**	**MIM grating, metal analyzer**
Advantage	CMOS compatible without postprocessing	High efficiency (29%)	Colour bandpass control Joint wavelength decoding Moderate effciency (2x12%, figure 4.12)
Disadvantages	Low efficiency (12%) Suffers from destructive internal reflection and roundtrip	Needs 1 postprocessing step Hard to integrate colour filter	Needs custom postprocess Suffers from destructive internal reflection and roundtrip

8

THESIS POSTULATION

To arrive at the presented results, the following essential research steps have been performed and documented in this thesis:

- Interest in lens-less imaging has been sparked due to its usefulness in imaging sensors for biomedical applications
- Limitations of the current solution have been identified
- Limitations have been verified in simulation
- Literature review has been conducted in search for a solution according to a set of specifications
- Candidate solution structure has been reproduced to verify claims in literature
- Limitations of the candidate structure have been investigated to review usefulness
- The full structure has been jointly fabricated, measured, and cross-validated by theory and simulation until meaningful results have been found
- A measurement setup has been designed, acquired and built according to measurement requirements
- Fabrication recipes have been formulated and constantly updated with new findings
- Limits of the device has been investigated and reviewed to initial specifications
- A use case is demonstrated to illustrate potential in large scale integration
- A final comparison with the initial structure is made to discuss outcome and added value of the research

To the best extend of my knowledge, this is the first report of two phenomena:

1. A wavelength scale colour filter grating creating two nonoverlapping independent talbot image (figure 4.8).

2. Colour sensitivity is added to the concept of angle sensitive pixel 4.11. Previously a source of distortion, multichromatic scenes are now a method for better image reconstruction.

Combining these brings me to postulation of my thesis which this document aims to defend.

By postprocessing a patterned nanophotonic Metal-Insulator-Metal structure that filters colour based on interference on top of a pixel array, lensless imaging in near-field scenario's takes a step forward by adding high Q-factor wavelength separation, opening a new dimension of distinguishability without compromising SNR.

9

FURTHER RESEARCH

The previous chapter concluded this thesis as a documentation of the completed MSc graduation research project. However, this thesis is just the start of a full-scale PhD research project. Any ideas presented in this chapter are not part of the thesis and are not proposed as true in any way.

MIM-ASP DEVICE IMPROVEMENTS

Building upon the drawbacks presented in chapter 7, recommendations for further research are formulated.

Fabrication The main established drawback of the MIM-ASP device is it difficulty of postprocessing. This limits large scale integration at competitive pricing, crucial because a main motivation for lensless imaging is the large market potential. Even if standardized materials such as aluminum can support a Fabry Perot cavity, the required thicknesses of a few nm are not standard. It can be further investigated what commercially available processes can handle similar materials at similar feature sizes. By reengineering the fabrication scheme, transmission efficiency can get closer to the ideal case.

Transmission Two ideas are conceived that could possibly improve transmission efficiency. Both are inspired by [7] and illustrated in figure 9.1.

- It can be investigated whether optical components such as MIM and phase gratings are linear components. This linearity implies the interchangability of the MIM grating and the analyzer grating. If that holds, the MIM grating can be used as the analyzer, and a phase grating can be implemented as the talbot image generating grating. See figure 9.1a.
- An analyzer grating could be discarded altogether. This could be done by interleaving photodiodes, and placing them at an optimal talbot depth. The difference

with the published interleaved photodiode is that these photodiodes could have a depth optimized for that specific wavelength. That configuration uses the photodiode's inherent spectral filtering to its advantage. It has to be investigated whether the smaller photodiode fill factor weighs up against the advantages.

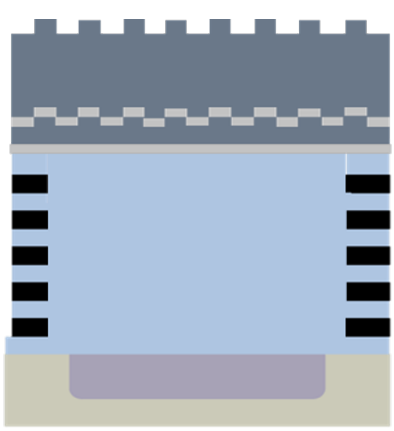

+ Improves the transmissivity by ~2x
- Increased height above metal stack decreases signal power near the dead angle

(a) Combination of phase grating and an MIM structure as analyzer grating

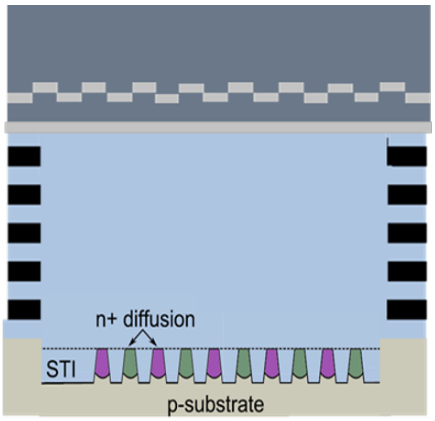

+ Improves the transmissivity even further
- Lowers m by increasing crosstalk
- Dependent on technology node

(b) Combination of MIM grating and interleaved diodes optimized for colour

Figure 9.1: Sketches of ideas for improvement of transmission efficiency of MIM-ASP structure. Both ideas are inspired by improvements for the ASP presented in [7]. The darker blue indicates oxide that is deposited during the custom postprocess, not by the CMOS manufacturer.

MIM-ASP ARRAY IMAGING IMPROVEMENTS

The computational imaging is barely touched upon in this thesis, and is the subject of a new line of research.

Furthermore, a set of ideas could be investigated:

- A least squares solution with regularization parameter on the 1-norm can be used. This method had been used for previous ASP projects [34].
- The joint classification, described in figure 6.6, can be implemented.
- Joint optimization of detector layout and reconstruction algorithm according to application specific assumption.

ACKNOWLEDGEMENTS

This chapter is devoted to closing statement, thanking people contbributing to the final result.

Before anyone else I thank my parents, Hans and Gitta, for their unconditional support of my journey. Even after almost seven years of studying in Delft, they helped me put the Columbia crown on my diploma. It was great fun having them visit five time the last year.

Emigrating to New York to perform research at Columbia University was a surprisingly wonderful experience. Starting out, I never saw myself devoting the second half of my twenties to doing research. But after approximately six months, I gratefully accepted the offer letter for the phd-programme extended to me by the same PI who offered me the masters thesis project, Ken Shepard.

This would never have happened hadn't I had the chance to work together with gifted researchers going by the names of Changhyuk Lee, Girish Ramakrishnan, Hyung-Sik Kim and David Gidony. Especially learning from Changhyuk was a steep and therefore enjoyable experience.

I would like to thank members the ASRC nanofabrication squad, Girish, Kukjoo, Jeffrey, Rizwan, Hyung-Sik and Jake, for assisting me in understanding nanofabrication and giving me countless small but essential tips.

My former roommate Duco Blanken, already a PhD candidate at TU Delft, helped me in countless instances until this date. Looking forward to becoming colleagues is just as fun as looking forward to keeping a competition of who will publish better and more.

I want to thank my fellow members of Club Priem for the majority of good memories of my time in Delft. I always had a lot of fun with and support from my fellow EE students at TU Delft: Paul Marcelis, Remco van der Plaats, Lennart Boeke, Bas van Wee, Ide Swager, Hendrik Pries, Patrick, Derk-Jan, Pascal, Rob, Leon, Moritz, Ralph, Sander, Lennart, Joris.

Futhermore, thanks go out to my buddies in the lacrosse team for body slamming and D-pole checking me after a long day in the office, reminding me to stay physically fit. I should not forget to thank my friends at Beta Theta Pi, for reminding me that I am still a student and providing a stable flux of fun events. And of course my Dutch friends Diederik and Liset, to remind me of the Dutch laid back way of living.

Special thanks goes out to Matthew Levine, my tennis buddy who helped me deciding on accepting the offer by listening to my concerns, a taboo within the halls of Columbia.

Last but not least thanks to my friends who visited me in New York, and to my friends who didn't visit: you only have five more years left, so hurry up!

A

ASP MEASUREMENT SETUP

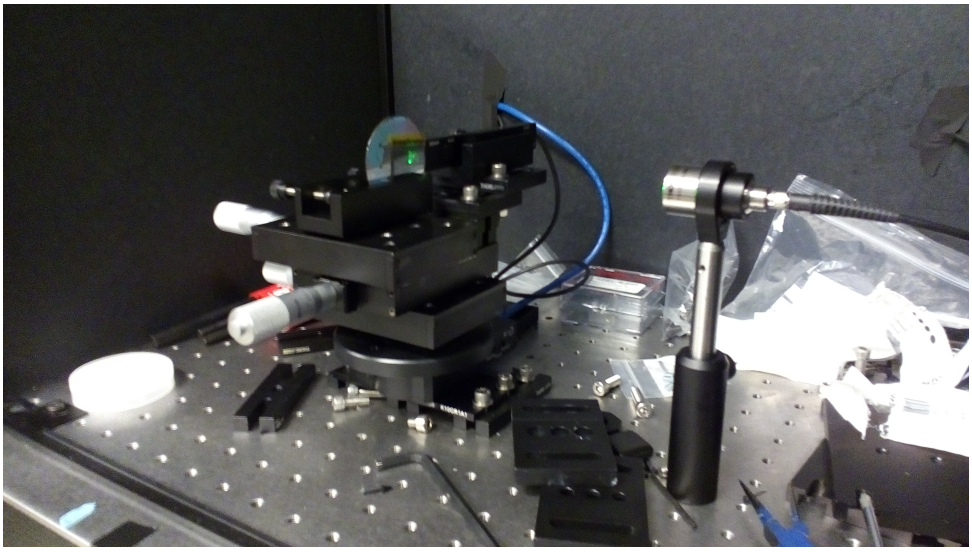

Figure A.1: Measurement setup for measuring the ASP function. The measurement setup was designed to mimic a photodiode postprocessed with a MIM-ASP structure, sweeping the angle of incident light.

B

POLARIZATION MEASUREMENT SETUP

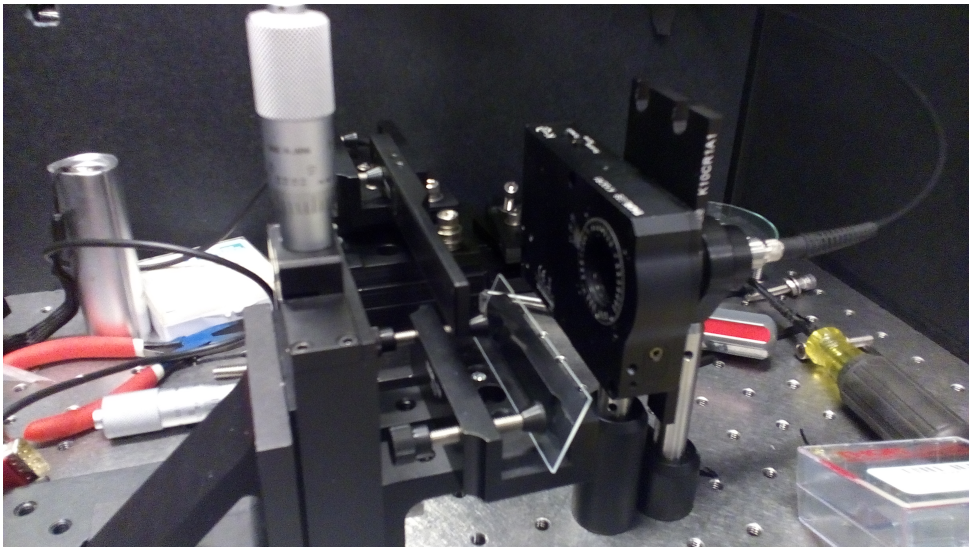

Figure B.1: Measurement setup for polarization effect on MIM grating transmission. Measurement is done by fixing the device while inserting a polarization filer into a rotational stage.

REFERENCES

[1] V. Boominatham, J. Adams, M. Asif, B. Avants, J. Robinson, R. Baraniuk, A. Sankaranarayanan, and A. Veeraraghavan, *Lensless imaging: A computational renaissance,* IEEE Signal Processing Magazine (2016).

[2] E. Charbon, *Imaging sensors,* ET4390 **Lecture 4** (2016).

[3] C. Lee, *In-vivo camera using single photon avalanche diode,* a **1**, 20 (2016).

[4] M. Cieslak, K. Gamage, and R. Glover, *Coded-aperture imaging systems: Past, present and future development – a review,* Radiation Measurements **92**, 59 (2016).

[5] G. Huang, H. Jiang, K. Matthews, and P. Wilford, *Lensless imaging by compressive sensing,* IEEE International Conference on Image Processing **128**, 2102 (1962).

[6] M. Asif, A. Ayremlou, A. Sankaranarayanan, A. Veeraraghavan, and R. Baraniuk, *Flatcam: Thin, bare-sensor cameras using coded aperture and computation,* arXiv:1509.00116v2 (2016).

[7] S. Sivaramakrishnan, A. Wang, P. Gill, and A. Molnar, *Design and characterization of enhanced angle sensitive pixels,* IEEE TRANSACTIONS ON ELECTRON DEVICES **63**, 113 (2016).

[8] J. Wen and M. Zhang, Y. Xiao, *The talbot effect: recent advances in classical optics, nonlinear optics, and quantum optics,* Advances in Optics and Photonics **5**, 83 (2013).

[9] M. Kim, C. Scharf, T. Menzel, C. Rockstuhl, and H. Herzig, *Talbot images of wavelength-scale amplitude gratings,* OPTICS EXPRESS **5**, 83 (2012).

[10] P. Gill, C. Lee, S. Sivaramakrishnan, and A. Molnar, *Robustness of planar fourier capture arrays to colour changes and lost pixels,* arXiv:arXiv:1111.4524v2 (2011).

[11] M. Hirsch, S. Sivaramakrishnan, S. Jayasuriya, A. Wang, A. Molnar, R. Raskar, and G. Wetzstein, *A switchable light field camera architecture with angle sensitive pixels and dictionary-based sparse coding,* IEEE ICCP (2014).

[12] Y. Yu, L. Wen, S. Song, and Q. Chen, *Review article: Transmissive/reflective structural color filters: Theory and applications,* Journal of Nanomaterials (2014).

[13] H. Koo, M. Chen, and P. Pan, *Lcd-based color filter films fabricated by a pigment-based colorant photo resist inks and printing technology,* Thin Solid Films **515**, 896 (2006).

[14] Q. Chen, D. Chitnis, K. Walls, T. Drysdale, S. Collins, and D. Cumming, *Cmos photodetectors integrated with plasmonic color filters,* IEEE Photonics Technology Letters **24**, 197 (2012).

[15] Z. Li, S. Butun, and K. Aydin, *Large-area, lithography-free super absorbers and color filters at visible frequencies using ultrathin metallic films,* ACS Photonics **2**, 183 (2015).

[16] Y. Yoon and S. Lee, *Transmission type color filter incorporating a silver film based etalon,* Optics Express **18**, 5344 (2010).

[17] B. Jafarian, N. Nozhat, and N. Grapayeh, *Analysis of a triangular-shaped plasmonic metal-insulator-metal bragg grating waveguide,* Journal of Optical Society of Korea **15**, 118 (2011).

[18] H. Ehrenreich and H. Philipp, *Optical properties of ag and cu,* Physical Review **128**, 1622 (1962).

[19] N. Christensen, *The band structure of silver and optical interband transisitons,* Phys. Stat. Sol. **54**, 551 (1972).

[20] A. Axelevitch, B. Gorenstein, and G. Golan, *Investigation of optical transmission in thin metal films,* Physics Procedia **32**, 1 (2012).

[21] S. Jayasuriya, S. Sivaramakrishnan, E. Chuang, D. Guruaribam, A. Wang, and A. Molnar, *Dual light field and polarization imaging using cmos diffractive image sensors,* Optics Letters **40**, 2433 (2015).

[22] A. Nesci, R. Dandliker, M. Salt, and H. Herzig, *Measuring amplitude and phase distribution of fields generated by gratings with sub-wavelength resolution,* Optics Communications **205**, 229 (2002).

[23] P. West, S. Ishii, G. Naik, K. Emani, V. Shalaev, and A. Boltasseva, *Searching for better plasmonic materials,* Laser Photonics Review **4**, 795 (2010).

[24] C. Langhammer, Z. Yuan, I. Zoric, and B. Kasemo, *Plasmonic properties of supported pt and pd nanostructures,* ACS Nanoletters **6**, 833 (2006).

[25] M. Rooks, E. Kratschmer, R. Viswanathan, J. Katine, R. Fontana, and S. MacDonald, *Low stress development of pmma for high aspect ratio structures,* Microelectronics and Nanometer Structures , 2937 (2002).

[26] V. Bhatt, S. Chandra, S. Kumar, C. Rauthan, and P. Dixt, *Stress evaluation of rf sputtered silicon dioxode films for mems,* Indian Journal of Pure and Applied Physics **45**, 377 (2007).

[27] A. Evans and J. Hutchinson, *The thermomechanical integrity of thin films and multilayers,* Acta Metallurgica **43**, 2507 (1995).

[28] T. Hodge, S. Bidstrup-Allen, and P. Kohl, *Stresses in thin film metallization,* IEEE Transactions on Components, Packaging, and Manufacturing Technology **20**, 241 (1997).

[29] N. Marechal, E. Quesnel, and Y. Pauleau, *Silver thin films deposited by magnetron sputtering,* Thin Solid Films **241**, 34 (1994).

[30] V. Nikolenko, K. Poskanzer, and R. Yuste, *Two-photon photostimulation and imaging of neural circuits,* Nature Methods **1105**, 1 (2007).

[31] C. Lee, S. Johnson, E. Chuang, D. Guruaribam, A. Wang, and A. Molnar, *A 72x60 angle sensitive spad imaging array for lens-less flim,* Sensors **16**, 1422 (2016).

[32] P. Inc, *Fluoresbrite microparticles, technical data sheet,* data sheet (2016).

[33] atdbio, *Bodipy dyes,* .

[34] P. Gill, A. Wang, and A. Molnar, *The in-crowd algorithm for fast basis pursuit denoising,* IEEE Transactions on Signal Processing **59**, 4595–4605 (2011).

[35] B. Zeng, Y. Gao, and F. Bartol, *Ultrathin nanostructured metals for highly transmissive plasmonic subtractive color filters,* Nature Scientific Reports **3**, 1 (2013).